

Structural, mechanical, and vibrational properties of particulate physical gels

Hideyuki Mizuno,^{1,*} Makoto Hachiya,¹ and Atsushi Ikeda^{1,2,†}

¹*Graduate School of Arts and Sciences, The University of Tokyo, Tokyo 153-8902, Japan*

²*Research Center for Complex Systems Biology, Universal Biology Institute,
The University of Tokyo, Tokyo 153-8902, Japan*

(Dated: September 28, 2021)

Our lives are surrounded by a rich assortment of disordered materials. In particular, glasses are well known as dense, amorphous materials, whereas gels exist in low-density, disordered states. Recent progress has provided a significant step forward in understanding the material properties of glasses, such as mechanical, vibrational, and transport properties. In contrast, our understanding of particulate physical gels is still highly limited. Here, using molecular dynamics simulations, we study a simple model of particulate physical gels, the Lennard-Jones (LJ) gels, and provide a comprehensive understanding of their structural, mechanical, and vibrational properties, all of which are markedly different from those of glasses. First, the LJ gels show sparse, heterogeneous structures, and the length scale ξ_s of the structures grows as the density is lowered. Second, the gels are extremely soft, with both shear G and bulk K moduli being orders of magnitude smaller than those of glasses. Third, many low-frequency vibrational modes are excited, which form a characteristic plateau with the onset frequency ω_* in the vibrational density of states. Structural, mechanical, and vibrational properties, characterized by ξ_s , G , K , and ω_* , respectively, show power-law scaling behaviors with the density, which establishes a close relationship between them. Throughout the present work, we reveal that gels are multiscale, solid-state materials: (i) homogeneous elastic bodies at long lengths, (ii) heterogeneous elastic bodies with fractal structures at intermediate lengths, and (iii) amorphous structural bodies at short lengths.

I. INTRODUCTION

Disordered materials are ubiquitous in our daily lives. Glasses are familiar examples at high density; examples include silicate glasses, metallic glasses, plastic materials, colloidal glasses, and so on [1–3]. In the glasses, particles are densely packed with disordered structures, and they behave as solids with rigidity. On the other hand, gels are disordered materials at low density, which can be categorized into polymeric gels that are composed of polymers with cross-linking [3–5] and particulate gels that are composed of particles such as colloids [3, 6–9].

In the gels, constituents are connected via bonds to form sparse heterogeneous network structures, such that they are of low density but still possess rigidity similar to solids. According to the nature of the bonds, gels can be classified into chemical gels and physical gels [4, 6]. In chemical gels, the bonds are chemical covalent bonds, which have virtually infinitely long lifetimes. As a result, chemical gelation is an irreversible process that has been analyzed using the percolation theory for the bonded network [5]. Around the gelation point, the static and dynamic elastic moduli exhibit critical scaling laws, which have also been analyzed by means of percolation theory [5].

On the other hand, in physical gels, the bonds between particles originate from physical interactions, such as van der Waals interactions and depletion interactions [3, 6–9]. The strengths of these bonds are much weaker than

those of covalent bonds (typically of the order of thermal energy $k_B T$, where T is temperature and k_B is Boltzmann's constant), and formation of the physical gels is reversible and can be controlled by changing the physical conditions. The present work concerns the material properties of particulate physical gels, with comparison to those of glasses.

Glasses are formed by lowering the temperature or increasing the density of particulate systems in their liquid states. During these processes, the relaxation dynamics become increasingly sluggish, and the system loses the ability to relax into an equilibrium state at some point and falls into a nonequilibrium solid state, which is called the glass transition [2]. The material properties of glasses are known to be widely different from those of crystalline solids [1]. Their elastic moduli are smaller than those of their counterparts in crystalline states due to non-affine deformations [10–13]. Additionally, they show a characteristic excess of low-frequency vibrations, which is called the Boson peak (BP) [14–16]. The nature of vibrational states is changed at the BP frequency ω_{BP} ; below ω_{BP} , phonon-like vibrational modes and quasi-localized vibrational (QLV) modes are observed [17–20], whereas above ω_{BP} , vibrational modes show highly disordered vibrations [18, 19, 21], which are called anomalous modes [22–24]. Note that jammed states of short-ranged, soft repulsive particles play an important role in studies of these anomalous properties of glasses because this model exhibits the critical behavior of shear modulus due to the non-affine deformations [25, 26] and abundance of the low-frequency vibrations, as evidenced in the flat vibrational density of state (vDOS) $g(\omega) \propto \omega^0$ above the BP [22–24, 27].

* hideyuki.mizuno@phys.c.u-tokyo.ac.jp

† atsushi.ikeda@phys.c.u-tokyo.ac.jp

Particulate physical gels are formed by increasing the relative importance of attractive interactions between constitutive particles at low density, e.g., by adding salt to weaken the repulsive electrostatic interactions or by adding non-adsorbing polymers to strengthen the depletion interactions [3, 6–9]. When the density of particles is very low ($\varphi \lesssim 0.1$, where φ is the packing fraction), attractive particles form fractal aggregates and ultimately become gels as the size of aggregates becomes macroscopic [28]. This gelation process has been understood as diffusion-limited aggregation (DLA), in which irreversible bonds are formed when two particles come into contact through diffusion processes [8, 29–31]. The elastic properties of DLA gels have been discussed in terms of percolation theory, as in the case of chemical gels, where the fractal dimension plays a key role in determining the scaling behaviors of the elastic moduli [28, 32–35].

When the density is increased to a moderately low regime ($\varphi \gtrsim 0.1$), gelation takes place through *arrested phase separation* [6, 8]. The equilibrium phase diagram of attractive particles includes gas and liquid phases, and the system undergoes gas-liquid phase separation when the attractive interaction is strong enough [36, 37]. However, when the attractive interaction is too strong, the equilibrium liquid phase cannot be realized because of the sluggish dynamics brought by the glass transition. In this situation, the phase separation is interrupted so that the system forms the interconnected network structure of clusters of glasses, which is the gel state [6, 8]. At the level of the phase diagram, this scenario has been quantitatively verified by a combination of experimental and theoretical studies [38]. However, the dynamics of this gelation process are not yet fully understood. Numerical simulations [39, 40] of the quenching of moderately low-density, attractive particles have demonstrated that such a system exhibits power-law growth of domain size in the short term followed by logarithmically slow long-term domain growth during the later stages. For short-term behavior, the importance of dynamic asymmetry has been pointed out very recently [41]. For long-term behavior, similarity to the aging dynamics in glassy systems was pointed out [40, 42], but there is currently no quantitative understanding. Furthermore, the mechanical properties of particulate physical gels are not yet understood and are under active debate [28]. Various kinds of scenarios and explanations have been proposed, including jamming transition [43], hierarchical arrest [44, 45], locally favoured structures [46], local isostaticity [47, 48], rigidity percolation [49], and a correlated version of the rigidity percolation [50].

In the present work, we provide a comprehensive understanding of the structural, mechanical, and vibrational properties of particulate physical gels that are formed via arrested phase separation. One particular focus is to discuss the similarity and difference between gels and glasses. To achieve this, we focus on the simplest model: the zero-temperature quench of the system composed of Lennard-Jones (LJ) particles. Thanks to recent

studies [10, 11, 13, 19], the mechanical and vibrational properties of LJ glasses are well understood, and we are now in a position to discuss the material properties of LJ gels based on comparing them to their glass counterparts. Although the LJ particles might not be used for modeling colloidal systems, we believe that the understanding of the LJ gels provides a good starting point to understand the properties of colloidal gels, thus taking advantage of utilizing a well-established understanding of their glass counterparts.

II. METHODS

A. System description

We have performed molecular dynamics (MD) simulations on a model system that shows the glass transition at high density and gelation through arrested phase separation at lower density. The system is composed of N point particles in three-dimensional ($d = 3$) space under periodic boundary conditions in all three directions. Particles i and j interact through the LJ potential:

$$\phi_{\text{LJ}}(r) = 4\epsilon \left[\left(\frac{\sigma_{ij}}{r} \right)^{12} - \left(\frac{\sigma_{ij}}{r} \right)^6 \right], \quad (1)$$

where r is the distance between these two particles, $\sigma_{ij} = (\sigma_i + \sigma_j)/2$, and σ_i is the size (diameter) of particle i . To avoid crystallization, we introduce a polydispersity in the distribution of particle sizes, as in Ref. [11]. Specifically, the values of σ_i ($i = 1, 2, \dots, N$) are uniformly distributed in a range of 0.8σ to 1.2σ . The potential is cut off at $r = r_c = 3\sigma$, where the potential and its first derivative are both made continuous as in [19]

$$\phi(r) = \phi_{\text{LJ}}(r) - \phi_{\text{LJ}}(r_c) - (r - r_c) \frac{d\phi_{\text{LJ}}(r_c)}{dr}. \quad (2)$$

The mass m is identical for all particles. In the following, we employ ϵ , σ , and $\tau = \sqrt{(m\sigma^2)/\epsilon}$ as units of energy, length, and time, respectively. The temperature and the frequency are measured by units of ϵ/k_B (k_B is Boltzmann's constant) and $\tau^{-1} = \sqrt{\epsilon/(m\sigma^2)}$, respectively.

To study both the glass state and gel state, we vary the number density $\rho = N/V$ ($V = L^3$ is the volume of the system, and L is the linear dimension of the system) in a wide range of $\rho = 1.0, 0.7, 0.5, 0.3, 0.2$ and 0.1 , where the corresponding packing fractions are $\varphi = (\rho\pi/6) \int_{0.8}^{1.2} (\sigma_i^3/0.4) d\sigma_i = 0.054, 0.11, 0.16, 0.27, 0.38$ and 0.54 , respectively. We also vary the number of particles N from $N = 10000$ to 640000 to study finite system-size effects and access lower-frequency vibrational modes.

We first equilibrated the system in the normal liquid state at a temperature of $T = 3.0$. We then quenched the system to the zero-temperature state of $T = 0$ by

minimizing the system potential and bringing the system to the local potential minimum. Here, we employ the steepest descent method [51] for minimization. We numerically judge that the system settles down to a local potential minimum when the maximum value f_{\max} of the forces \mathbf{F}_i that act on particles i ($i = 1, 2, \dots, N$) falls below 10^{-9} . Note that this protocol corresponds to an instantaneous quenching process with an infinite quenching rate.

In the following, we denote the $T = 0$ configuration of particles (or the inherent structure) as $\mathbf{r} = [\mathbf{r}_1, \mathbf{r}_2, \dots, \mathbf{r}_N]$ ($3N$ -dimensional vector), where \mathbf{r}_i is the position of particle i . As will be demonstrated in Sec. III, we obtain the glass configuration at $\rho = 1.0$, while for the cases of $\rho = 0.7, 0.5, 0.3$ and 0.2 , we observe the gel configurations that are realized through arrested phase separation.

B. Structural properties

We now obtained the $T = 0$ configurations of particles, $\mathbf{r} = [\mathbf{r}_1, \mathbf{r}_2, \dots, \mathbf{r}_N]$, at different densities ρ . We first characterized the static structural properties of these configurations by calculating the radial distribution function $g(r)$ and the static structure factor $S(q)$ [52]. We also measured the integrated value of $g(r)$, $N(r)$, as

$$N(r) = \int_0^r 4\pi r'^2 \rho g(r') dr'. \quad (3)$$

Since $g(r)$ behaves as $g(r) \simeq 1$ at long distances $r \gg 1$, $N(r)$ converges to $\simeq (4\pi\rho/3)r^3 \propto r^3$. This behavior of $N(r) \propto r^3$ ($= r^d$) indicates homogeneous media. In contrast, $N(r) \propto r^{D_f}$ with the exponent of $D_f < 3$ ($= d$) suggests sparse and heterogeneous structure or fractal-like structure, where D_f is the fractal dimension [53].

C. Vibrational properties

We next performed vibrational mode analysis on the $T = 0$ configurations [54, 55]. We solved the eigenvalue problem of the dynamical matrix \mathbf{D} ($3N \times 3N$ matrix) to obtain the eigenvalues λ_k and the corresponding eigenvectors $\mathbf{e}^k = [\mathbf{e}_1^k, \mathbf{e}_2^k, \dots, \mathbf{e}_N^k]$ for the modes $k = 1, 2, \dots, 3N - 3$ (3 zero-frequency, translational modes are removed). The eigenvectors are orthonormalized as $\mathbf{e}^k \cdot \mathbf{e}^l = \sum_{i=1}^N \mathbf{e}_i^k \cdot \mathbf{e}_i^l = \delta_{k,l}$, where $\delta_{k,l}$ is the Kronecker delta function.

In the gels with $\rho = 0.2$ and 0.3 , we found several vibrational modes with a zero eigenvalue, $\lambda_k = 0$. These modes with zero-energy cost emerge in clusters of particles that are isolated from the network structure of gels (see Sec. V F for details). We denote the number of these zero-frequency modes as N' . In analyses of the present work, these modes are disregarded.

We analyzed several different system sizes of $N = 10000$ to 640000 [56]. We first calculated all the vibrational modes in the smallest system of $N = 10000$. We then calculated the low-frequency modes in the larger systems of $N = 20000$ to 640000 . Finally, the modes obtained from different system sizes were combined as a function of the frequency ω_k . We found that the results from different system sizes smoothly connect with each other, which enables us to extend the mode information to the lower-frequency regime [18]. In the figures of this paper, all data from different system sizes are presented together.

1. Vibrational density of states

From the dataset of eigenfrequencies, $\omega_k = \sqrt{\lambda_k}$ ($k = 1, 2, \dots, 3N - 3 - N'$), the vibrational density of states (vDOS) is calculated as

$$g(\omega) = \frac{1}{3N - 3 - N'} \sum_{k=1}^{3N-3-N'} \delta(\omega - \omega_k), \quad (4)$$

where $\delta(x)$ is the Dirac delta function. We have calculated the vDOSs by using different system sizes, which smoothly connect and give values in a wider (lower) frequency regime (see Fig. S1 in the Supplementary Material (SM)).

As will be described in Sec. II D, we measured the bulk modulus K and the shear modulus G_0 . From these values of elastic moduli, we calculated the Debye frequency ω_D and the Debye level A_D , as

$$\omega_D = \left[\frac{18\pi^2 \rho}{(c_L^{-3} + 2c_T^{-3})} \right]^{1/3}, \quad (5)$$

$$A_D = \frac{3}{\omega_D^3},$$

where $c_L = \sqrt{(K + 4G_0/3)/\rho}$ and $c_T = \sqrt{G_0/\rho}$ are longitudinal and transverse sound speeds, respectively. We note that the ‘‘minimum’’ value of shear moduli G_0 is employed for the calculation of these Debye values.

2. Phonon order parameter

The phonon order parameter O_k evaluates the extent to which eigenvector $\mathbf{e}^k = [\mathbf{e}_1^k, \mathbf{e}_2^k, \dots, \mathbf{e}_N^k]$ of the mode k is similar to phonon vibrations [18, 19]. We first define the displacement vectors of phonon vibrations as $\mathbf{e}^{\mathbf{q},\alpha} = [\mathbf{e}_1^{\mathbf{q},\alpha}, \mathbf{e}_2^{\mathbf{q},\alpha}, \dots, \mathbf{e}_N^{\mathbf{q},\alpha}]$ with

$$\mathbf{e}_i^{\mathbf{q},\alpha} = \frac{1}{\sqrt{N}} \mathbf{s}_\alpha(\hat{\mathbf{q}}) \exp(i\mathbf{q} \cdot \mathbf{r}_i), \quad (6)$$

where \mathbf{q} represents the wave vector, $\hat{\mathbf{q}} = \mathbf{q}/|\mathbf{q}|$, and α denotes one longitudinal ($\alpha = L$) and two transverse

($\alpha = T_1, T_2$) phonon modes. $\mathbf{s}_\alpha(\hat{\mathbf{q}})$ is a unit vector that represents the direction of polarization: $\mathbf{s}_L(\hat{\mathbf{q}}) = \hat{\mathbf{q}}$ (longitudinal) and $\mathbf{s}_{T_1}(\hat{\mathbf{q}}) \cdot \hat{\mathbf{q}} = \mathbf{s}_{T_2}(\hat{\mathbf{q}}) \cdot \hat{\mathbf{q}} = 0$ (transverse).

We then define the phonon order parameter O_k as

$$O_k = \sum_{\mathbf{q}, \alpha; O_k^{\mathbf{q}, \alpha} \geq N_m / (3N - 3 - N')} O_k^{\mathbf{q}, \alpha}, \quad (7)$$

$$O_k^{\mathbf{q}, \alpha} = |\mathbf{e}^{\mathbf{q}, \alpha} \cdot \mathbf{e}^k|^2 = \left| \sum_{i=1}^N \mathbf{e}_i^{\mathbf{q}, \alpha} \cdot \mathbf{e}_i^k \right|^2,$$

where $N_m = 100$ is employed; however, we confirm that our results and conclusions do not depend on the choice of the value of N_m [18, 19]. $O_k \approx 0$ indicates a mode considerably different from phonon vibrations, whereas finite values of $O_k > 0$ indicate phonon-like vibrations.

Here, we note that $\mathbf{e}^{\mathbf{q}, \alpha}$ does *not* necessarily satisfy the orthonormal condition; $\mathbf{e}^{\mathbf{q}, \alpha} \cdot \mathbf{e}^{\mathbf{q}', \alpha'} = \sum_{i=1}^N \mathbf{e}_i^{\mathbf{q}, \alpha} \cdot \mathbf{e}_i^{\mathbf{q}', \alpha'} \neq \delta_{\mathbf{q}, \mathbf{q}'} \delta_{\alpha, \alpha'}$, due to heterogeneous and amorphous structures, particularly for the gel configurations (for the glass, the orthonormal condition is approximately satisfied [18, 19]). Thus, it is possible that the value of O_k exceeds one, $O_k > 1$, which is indeed observed in the gels (see Fig. 9 and also Fig. S4 in SM).

3. Participation ratio

The participation ratio P_k quantitatively measures the extent of localization for each mode k , which has often been employed in many early works [57–59]. Given the eigenvector $\mathbf{e}^k = [\mathbf{e}_1^k, \mathbf{e}_2^k, \dots, \mathbf{e}_N^k]$, its participation ratio P_k is calculated as

$$P_k \equiv \frac{1}{N} \left[\sum_{i=1}^N (\mathbf{e}_i^k \cdot \mathbf{e}_i^k)^2 \right]^{-1}. \quad (8)$$

P_k quantifies the fraction of particles that participate in the vibrations (NP_k quantifies the number of participating particles) [57–59]. As extreme cases, $P_k = 1$ ($NP_k = N$) for an ideal mode in which all the constituent particles vibrate equally, and $P_k = 1/N \ll 1$ ($NP_k = 1$) for an ideal mode involving only one particle.

4. Vibrational energy

We also calculated the vibrational energies of δE_k^{\parallel} and δE_k^{\perp} for each mode k [18, 60, 61]. The vector of $\mathbf{e}_{ij}^k = \mathbf{e}_i^k - \mathbf{e}_j^k$ represents the vibrational motion between particles i and j , which can be decomposed into the normal $\mathbf{e}_{ij}^{k\parallel}$ and tangential $\mathbf{e}_{ij}^{k\perp}$ vibrations with respect to the bond vector $\mathbf{n}_{ij} = (\mathbf{r}_i - \mathbf{r}_j) / |\mathbf{r}_i - \mathbf{r}_j|$; $\mathbf{e}_{ij}^{k\parallel} = (\mathbf{e}_{ij}^k \cdot \mathbf{n}_{ij}) \mathbf{n}_{ij}$ and $\mathbf{e}_{ij}^{k\perp} = \mathbf{e}_{ij}^k - (\mathbf{e}_{ij}^k \cdot \mathbf{n}_{ij}) \mathbf{n}_{ij}$. Accordingly, the vibrational

energy $\delta E_k = \lambda_k/2 = \omega_k^2/2$ can be decomposed as

$$\delta E_k = \sum_{\langle ij \rangle} \left[\frac{\phi''(r_{ij})}{2} (\mathbf{e}_{ij}^{k\parallel})^2 + \frac{\phi'(r_{ij})}{2r_{ij}} (\mathbf{e}_{ij}^{k\perp})^2 \right], \quad (9)$$

$$= \delta E_k^{\parallel} - \delta E_k^{\perp},$$

where $\sum_{\langle ij \rangle}$ denotes summation over all the interacting pairs of particles $\langle ij \rangle$. If the mode k is phonon-like, then δE_k^{\parallel} and δE_k^{\perp} are both proportional to $\delta E_k \propto \omega_k^2$ [18]. For the QLV modes and anomalous modes (disordered vibrations) in glasses, the tangential energy δE_k^{\perp} exhibits ω_k -independent behavior, and $\delta E_k^{\perp} \propto \omega_k^0$ [18, 60].

5. Spatial correlation of displacement field

To study spatial correlations of the displacement field in the vibrational mode k , we have calculated the correlation function $C_k(r)$ [21]:

$$C_k(r = r_{ij}) = \langle \mathbf{e}_i^k(\mathbf{r}_i) \cdot \mathbf{e}_j^k(\mathbf{r}_j) \rangle_{ij}, \quad (10)$$

where $\mathbf{e}_i^k(\mathbf{r}_i)$ of particle i is denoted as a function of the position \mathbf{r}_i , and $r = r_{ij} = |\mathbf{r}_i - \mathbf{r}_j|$, and $\langle \rangle_{ij}$ denotes the average over all the pairs of particles ij . The phonon vibrations show long-range spatial correlations in $C_k(r)$. Particularly, for the transverse phonons, negative correlations are observed due to the vortex-like displacement field [62]. In contrast, anomalous modes in glasses show only short-range correlations with the order of particle size, representing disordered vibrations in nature [21].

D. Elastic moduli

We finally analyzed the mechanical properties of the $T = 0$ configurations, $\mathbf{r} = [\mathbf{r}_1, \mathbf{r}_2, \dots, \mathbf{r}_N]$, at different densities ρ . We calculated elastic moduli by using the fluctuation formulation developed based on linear response theory [63, 64]. Below, we write down the equations only and refer to Refs. [55, 60] for details of the explicit formulations.

The elastic modulus tensor $C_{\alpha\beta\gamma\delta}$ ($\alpha, \beta, \gamma, \delta = x, y, z$) is composed of affine modulus $C_{\alpha\beta\gamma\delta}^A$ and non-affine modulus $C_{\alpha\beta\gamma\delta}^N$, as

$$C_{\alpha\beta\gamma\delta} = C_{\alpha\beta\gamma\delta}^A - C_{\alpha\beta\gamma\delta}^N. \quad (11)$$

The affine $C_{\alpha\beta\gamma\delta}^A$ is formulated as

$$C_{\alpha\beta\gamma\delta}^A = C_{\alpha\beta\gamma\delta}^B + C_{\alpha\beta\gamma\delta}^C,$$

$$C_{\alpha\beta\gamma\delta}^B = \frac{1}{V} \sum_{\langle ij \rangle} \left(r_{ij}^2 \frac{d^2 \phi(r_{ij})}{dr_{ij}^2} - r_{ij} \frac{d\phi(r_{ij})}{dr_{ij}} \right) \times n_{ij\alpha} n_{ij\beta} n_{ij\gamma} n_{ij\delta}, \quad (12)$$

$$C_{\alpha\beta\gamma\delta}^C = -\frac{1}{2} (2\sigma_{\alpha\beta} \delta_{\gamma,\delta} - \sigma_{\alpha\gamma} \delta_{\beta,\delta} - \sigma_{\alpha\delta} \delta_{\beta,\gamma} - \sigma_{\beta\gamma} \delta_{\alpha,\delta} - \sigma_{\beta\delta} \delta_{\alpha,\gamma}),$$

where $n_{ij\alpha}$ represents the bond vector, $\mathbf{n}_{ij} = (\mathbf{r}_i - \mathbf{r}_j)/|\mathbf{r}_i - \mathbf{r}_j|$, and $\sigma_{\alpha\beta}$ is the stress tensor that is formulated as

$$\sigma_{\alpha\beta} = \frac{1}{V} \sum_{\langle ij \rangle} \left(r_{ij} \frac{d\phi(r_{ij})}{dr_{ij}} \right) n_{ij\alpha} n_{ij\beta}. \quad (13)$$

Note that $C_{\alpha\beta\gamma\delta}^B$ is the so-called Born term. In addition,

$$\begin{aligned} K &= \frac{(C_{xxxx} + C_{yyyy} + C_{zzzz} + C_{xxyy} + C_{yyxx} + C_{xxzz} + C_{zzxx} + C_{yyzz} + C_{zzyy})}{9}, \\ G_1 &= \frac{(C_{xxxx} + C_{yyyy} - C_{xxyy} - C_{yyxx})}{4}, \\ G_2 &= \frac{(C_{xxxx} + C_{yyyy} + 4C_{zzzz} + C_{xxyy} + C_{yyxx} - 2C_{xxzz} - 2C_{zzxx} - 2C_{yyzz} - 2C_{zzyy})}{12}, \\ G_3 &= C_{xyxy}, \quad G_4 = C_{xzxz}, \quad G_5 = C_{yzyz}. \end{aligned} \quad (15)$$

We note that for the shear modulus G , there are five independent values of G_1, G_2, G_3, G_4, G_5 . G_1 and G_2 are under *pure* shear deformations (plane strain and triaxial), and G_3, G_4 , and G_5 are under *simple* shear deformations. These five values are the same in isotropic systems, whereas they can be different in anisotropic systems in general. Indeed, we will observe anisotropic elastic properties with different values of shear modulus components in the gels (see Fig. S3 in SM). In this work, we define two values of shear moduli: average value G_{ave} and minimum value G_0 , as

$$\begin{aligned} G_{\text{ave}} &= \frac{(G_1 + G_2 + G_3 + G_4 + G_5)}{5}, \\ G_0 &= \min(G_1, G_2, G_3, G_4, G_5). \end{aligned} \quad (16)$$

III. STRUCTURAL PROPERTIES

A. Snapshot of system

Figure 1 visualizes the $T = 0$ configurations in three-dimensional space for densities of $\rho = 0.1, 0.2, 0.3, 0.5, 0.7$, and 1.0 . For the highest $\rho = 1.0$, we obtain the glass configuration. In the glass, particles are tightly packed, and the glass structure is disordered

the non-affine $C_{\alpha\beta\gamma\delta}^N$ is formulated as

$$C_{\alpha\beta\gamma\delta}^N = \sum_{k=1}^{3N-3-N'} \frac{V}{\omega_k^2} \left(\sum_{i=1}^N \frac{\partial \sigma_{\alpha\beta}}{\partial \mathbf{r}_i} \cdot \mathbf{e}_i^k \right) \left(\sum_{j=1}^N \frac{\partial \sigma_{\gamma\delta}}{\partial \mathbf{r}_j} \cdot \mathbf{e}_j^k \right), \quad (14)$$

where we remind the reader that N' zero-frequency modes appearing in gels are disregarded in the analysis, since they should make no contributions to the non-affine moduli.

From the modulus tensor $C_{\alpha\beta\gamma\delta}$, we have calculated two kinds of elastic moduli: bulk modulus K for volume-changing bulk deformation and shear modulus G for volume-preserving shear deformation, which are calculated as

but spatially homogeneous. As the density is lowered to $\rho = 0.7$ to 0.2 , the system undergoes phase separation between gas and glass during the rapid quenching process [39, 40], which results in sparse and heterogeneous configurations at $T = 0$. We note that $\rho = 0.2$ to 0.7 at $T = 0$ lies within the spinodal line of phase separation between gas and liquid [65]. Particularly, for the case of $\rho = 0.2$, we observe a rather heterogeneous, network-like structure where clusters of particles are connected with each other. Finally, for the lowest $\rho = 0.1$, the density is so low that the network structure is sufficiently broken down to be disconnected. In this state, isolated clusters of particles are distributed in space.

B. Characterization of structural properties

To characterize structural properties quantitatively, we present the radial distribution function $g(r)$ in Fig. 2(a) and the static structure factor $S(q)$ in Fig. 2(b). At $\rho = 1.0$, we observe characteristics of the glasses: $g(r)$ shows spatial correlation only at particle sizes of $r \sim 1$, and accordingly, $S(q)$ shows density fluctuations only at approximately $q \sim 2\pi$. As the density decreases towards $\rho = 0.2$, $g(r)$ shows the long-range correlations, and accordingly significant enhancement of $S(q)$ emerges at small wavenumbers q . These results of $g(r)$ and $S(q)$ quantify the heterogeneous structures visualized in Fig. 1.

As the density is lowered from $\rho = 1.0$ to 0.7 , a pre-

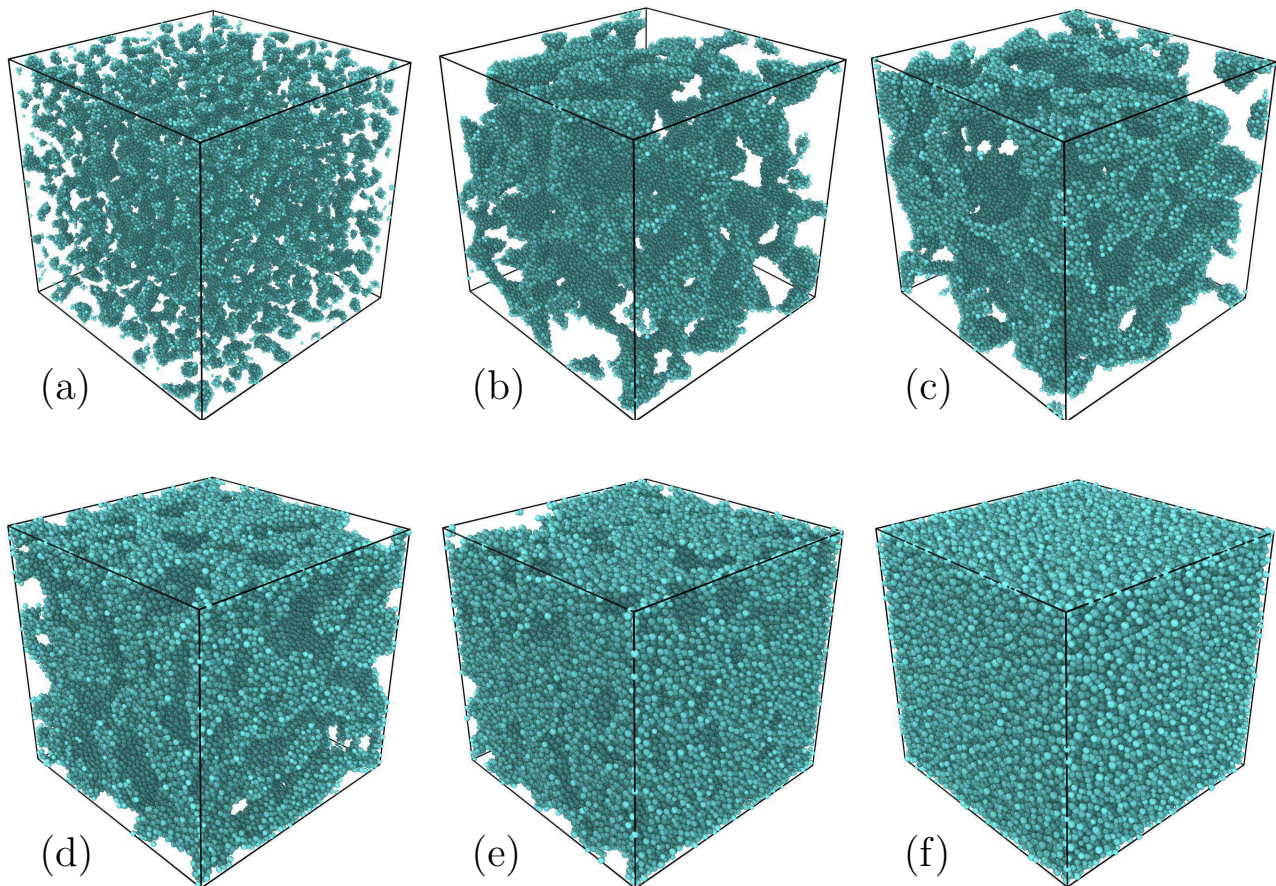


FIG. 1. Snapshot of the system. The $T = 0$ configurations are visualized for (a) $\rho = 0.1$ ($\varphi = 0.054$), (b) 0.2 (0.11), (c) 0.3 (0.16), (d) 0.5 (0.27), (e) 0.7 (0.38), and (f) 1.0 (0.54). The number of particles is $N = 80000$, and the system length is (a) $L = 92.8$, (b) 73.7, (c) 64.4, (d) 54.3, (e) 48.5, and (f) 43.1.

capituous shift is observed in $S(q)$ in Fig. 2(b). This behavior is attributed to spinodal decomposition (between gas and glass phases) at $T = 0$. Previous works demonstrated that the glass system at $T = 0$ experiences spinodal instability when lowering the density [66–68]. This observation is consistent with that the $T = 0$ systems of $\rho = 0.2$ to 0.7 are the gel states that are generated through arrested phase separation.

When examining $S(q)$ of $\rho = 0.2$ to 0.7 (gels) in more detail, we find that at $q \sim 0.8$ to 3, $S(q)$ follows the so-called Porod law [69], $S(q) \propto q^4$, indicating that the density field has sharp interfaces. This confirms that tightly packed particles form clusters and that such dense clusters are connected with each other to form a heterogeneous, network-like structure. Since $S(q)$ values at large $q \sim 2\pi$ (order of particle size) are similar to those of $\rho = 1.0$ (glass), clusters are in glass-solid states. At $q \lesssim 0.8$ and $\rho = 0.2$ and 0.3, we observe that $S(q)$ roughly follows $\propto q^{-2}$, and this scaling regime extends to the smaller q with ρ declining from 0.3 to 0.2. This result implies the existence of a fractal character of dimension $D_f \simeq 2$ [53, 70]. For the lowest $\rho = 0.1$, the connections of these clusters disappear, and they become isolated in

space, as visualized in Fig. 1. The values of $S(q)$ at small q are reduced, which means that the distribution of these isolated clusters tends to be homogeneous.

C. Characteristic length

We next present the integrated value of $g(r)$, $N(r)$, in Fig. 3 (see also Fig. S2 in SM). At long distances, it is observed that $N(r) \simeq (4\pi\rho/3)r^3 \propto r^3$ ($= r^d$), which crosses over to $N(r) \propto r^{D_f}$ with an exponent of $D_f < 3$ at intermediate distances for the gel configurations of $\rho = 0.2$ to 0.7. The exponent D_f decreases from $\simeq 3$ to $\simeq 2$ with decreasing density ρ : $D_f = 2.9, 2.7, 2.4, 2.2$ for $\rho = 0.7, 0.5, 0.3, 0.2$ (see Fig. S2 in SM). These results indicate that a fractal-like structure is developed at intermediate distances in the gels [53, 70]. The values of $D_f \simeq 2$ for $\rho = 0.2$ and 0.3 are consistent with the scaling of the static structure factor, $S(q) \propto q^{-2}$, observed in Fig. 2(b).

For the gels with $\rho = 0.2$ to 0.7, we define a characteristic length ξ_s as the onset distance of $N(r) \simeq (4\pi\rho/3)r^3 \propto r^3$. At $r < \xi_s$, $N(r) \propto r^{D_f}$ with $D_f < 3$, indicat-

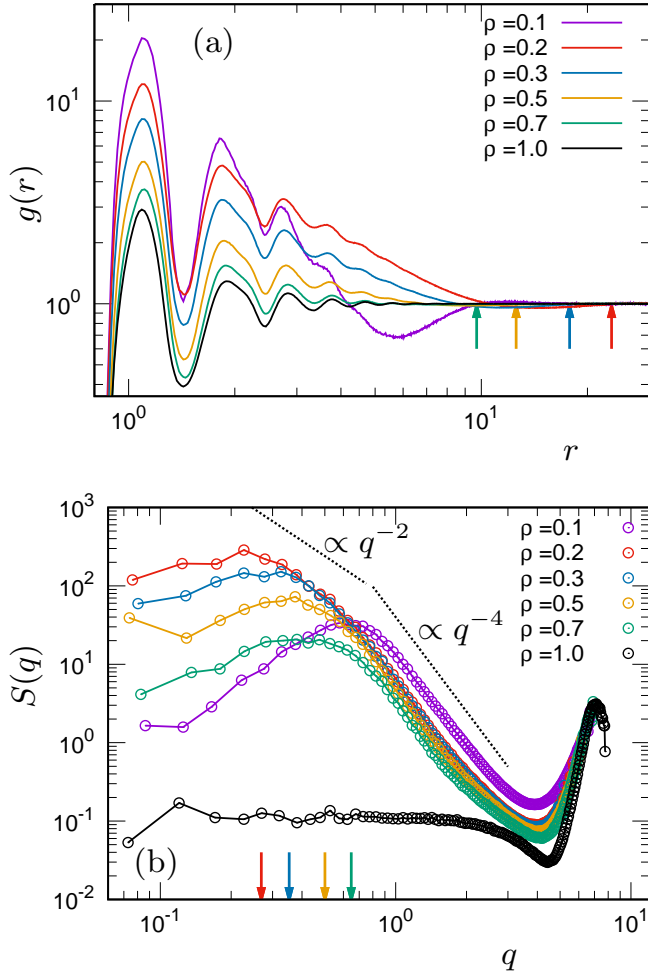


FIG. 2. Characterization of structural properties. (a) Radial distribution function $g(r)$ and (b) static structure factor $S(q)$ are plotted as functions of distance r and wavenumber q , respectively, for the indicated values of ρ . The arrows indicate the length ξ_s in (a) and the wavenumber $q_s = 2\pi/\xi_s$ in (b) for $\rho = 0.2, 0.3, 0.5, 0.7$. The dotted lines in (b) indicate the scaling of $S(q) \propto q^{-2}$ and the Porod law of $S(q) \propto q^{-4}$. Note that ξ_s is determined from the integrated value of $g(r)$, $N(r)$, as in Fig. 3.

ing sparseness and heterogeneities, whereas at $r > \xi_s$, $N(r) \propto r^3$, indicating that heterogeneities are coarse-grained and that the structure becomes homogeneous. For reference, Figure 2 plots the arrow values of ξ_s in (a) and the corresponding wavenumber $q_s = 2\pi/\xi_s$ in (b). We observe that $g(r)$ converges to 1 without oscillatory behavior at $r \geq \xi_s$, and correspondingly, $S(q)$ converges to flat behavior at $q \leq q_s$.

Finally, we plot the length ξ_s as a function of ρ in Fig. 4. The length grows with decreasing ρ , representing growing heterogeneities that are consistent with snapshots in Fig. 1. Remarkably, the length follows a power-law scaling of

$$\xi_s \propto \rho^{-0.7}. \quad (17)$$

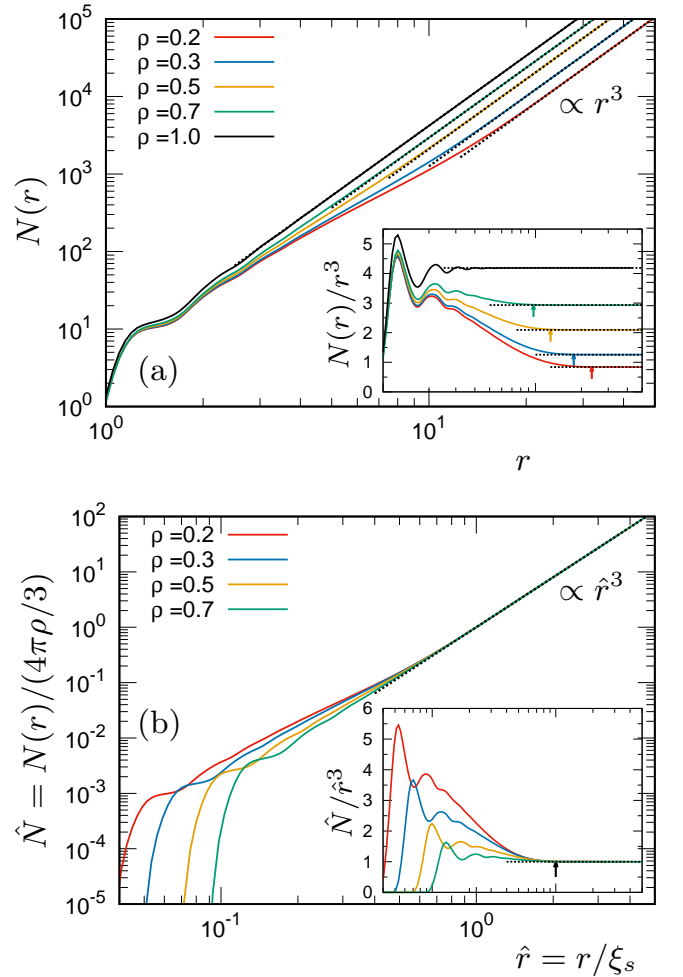


FIG. 3. Integrated value of radial distribution function. (a) $N(r)$ and (b) normalized $\hat{N} = N(r)/(4\pi\rho/3)$ are plotted as functions of r and $\hat{r} = r/\xi_s$, respectively, for the indicated values of ρ . We also present data of $N(r)/r^3$ and \hat{N}/\hat{r}^3 in the insets of (a) and (b), respectively. The length ξ_s is determined as the distance above which $N(r)$ follows the $N(r) = (4\pi\rho/3)r^3 \propto r^3$ scaling law, which is indicated by dotted lines. In the insets, arrows indicate values of length ξ_s .

This observation implies the existence of a critical phenomenon with the critical point at $\rho = 0$. We will discuss this point at the end of this paper in Sec. VI, after presenting all of the results regarding mechanical and vibrational properties.

D. Finite size effects

Finally, we mention the system-size effects on static structures. Figure 5 plots the static structure factor $S(q)$ for different system sizes of $N = 10000$ to 640000 . No noticeable differences are recognized between different system sizes. We therefore conclude that the heterogeneous structures of the gels are not affected by finite-system-

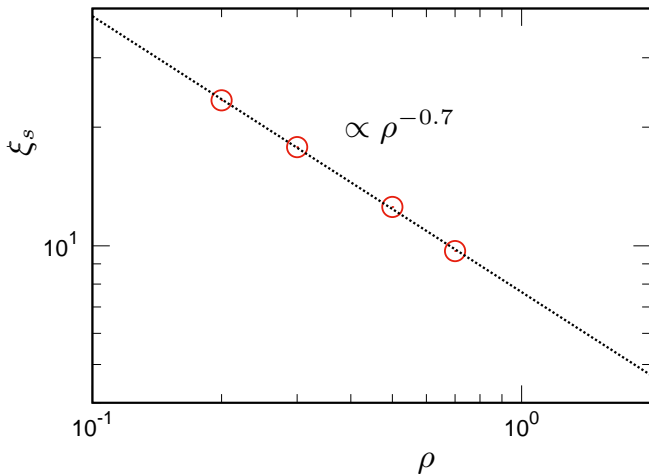


FIG. 4. Characteristic length in static structure. The length ξ_s is plotted as a function of ρ . The line indicates a power-law scaling of $\xi_s \propto \rho^{-0.7}$.

size effects. This result establishes that the characteristic length ξ_s remains finite even at the thermodynamic limit of $N \rightarrow \infty$ in the $T = 0$ quenching of systems; namely, the phase separation in this protocol is indeed arrested, and the LJ systems form well-defined gel states.

IV. MECHANICAL PROPERTIES

Figure 6 plots the shear modulus G (G_{ave}, G_0) in (a) and the bulk modulus K in (b) as functions of ρ . We first remark that the glass with $\rho = 1.0$ shows isotropic shear elasticity with nearly the same values of G_1 to G_5 , and so $G_{\text{ave}} \simeq G_0$. However, in the gels, the shear moduli become anisotropic with different values of G_1 to G_5 , as shown in Fig. S3 of SM. In Fig. 6, we find differences between G_{ave} and G_0 with lowering ρ . We expect that this anisotropy originates from the sparse, heterogeneous structures of gels.

As ρ is lowered, G and K decrease significantly and similarly. Comparing $\rho = 0.2$ (gel) and 1.0 (glass), the moduli of gels are orders of magnitude smaller than those of glasses; $G_{\text{ave}} = 0.22$, $G_0 = 0.13$, $K = 0.36$ at $\rho = 0.2$ and $G_{\text{ave}} \approx G_0 = 14$, $K = 65$ at $\rho = 1.0$. This result demonstrates that gels are extremely soft under both shear and bulk deformations. In Fig. 6, the affine and non-affine components are also presented. For amorphous systems, the non-affine moduli are important components to determine the elastic moduli [10–13]. As ρ is lowered, the affine G_A and K_A are nearly canceled by the non-affine G_N and K_N , respectively, which results in very small values of $G = G_A - G_N$ and $K = K_A - K_N$.

Note that the non-affine component K_N in bulk modulus is contrasting between gels and glasses. In the glasses, K_N is negligible compared to the affine K_A , $K_N \ll K_A$, and $K \approx K_A$ [11, 13]. Since particles are homogeneously packed in the glasses, their displacements under isotropic

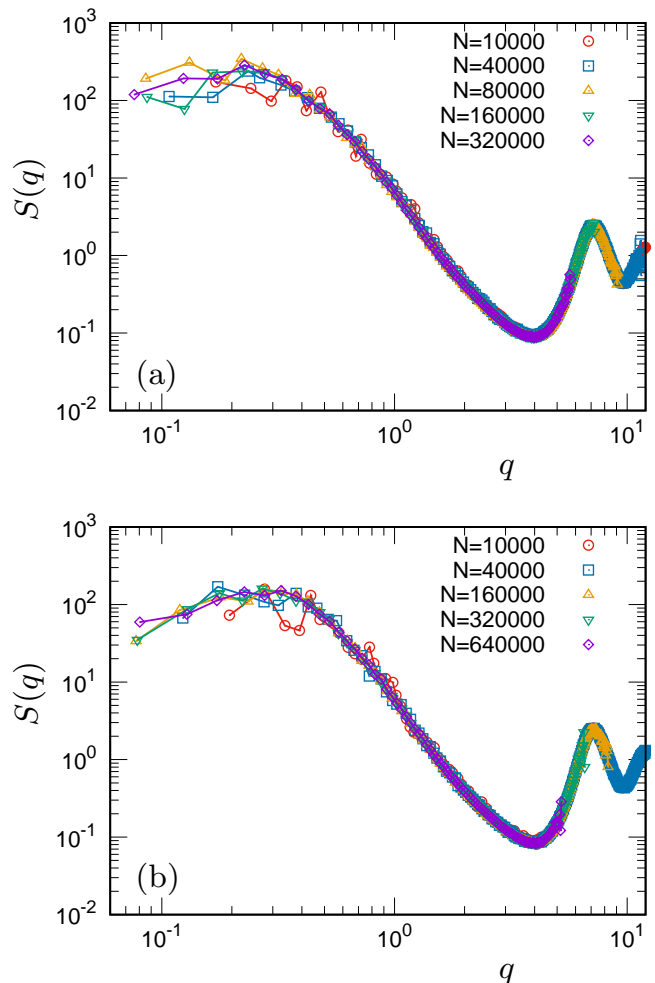


FIG. 5. Finite system-size effects on static structure factor. $S(q)$ is plotted as a function of q for different system sizes of $N = 10000$ to 640000. The density values are (a) $\rho = 0.2$ and (b) 0.3. No noticeable differences are observed between different system sizes.

bulk deformation are approximately along the affine deformation. In contrast, K_N is comparable to K_A in the gels. Due to the sparse and heterogeneous structures, non-affine motions of particles are induced in the gels even under isotropic deformation.

It is remarkable that G and K of the gels are observed to follow power-law scalings of

$$G_{\text{ave}} \propto \rho^{2.5}, \quad G_0 \propto \rho^{2.8}, \quad K \propto \rho^{2.5}. \quad (18)$$

The affine components also follow power-law scalings of $G_A \propto \rho^{1.0}$, $K_A \propto \rho^{1.0}$, which is simply because the system becomes sparse with lowering density. To eliminate effects from reductions in affine components, we can consider the scalings of

$$\frac{G_{\text{ave}}}{G_A} \propto \rho^{1.5}, \quad \frac{G_0}{G_A} \propto \rho^{1.8}, \quad \frac{K}{K_A} \propto \rho^{1.5}, \quad (19)$$

which are rather nontrivial scalings due to the non-affine deformations. This observation again implies the exist-

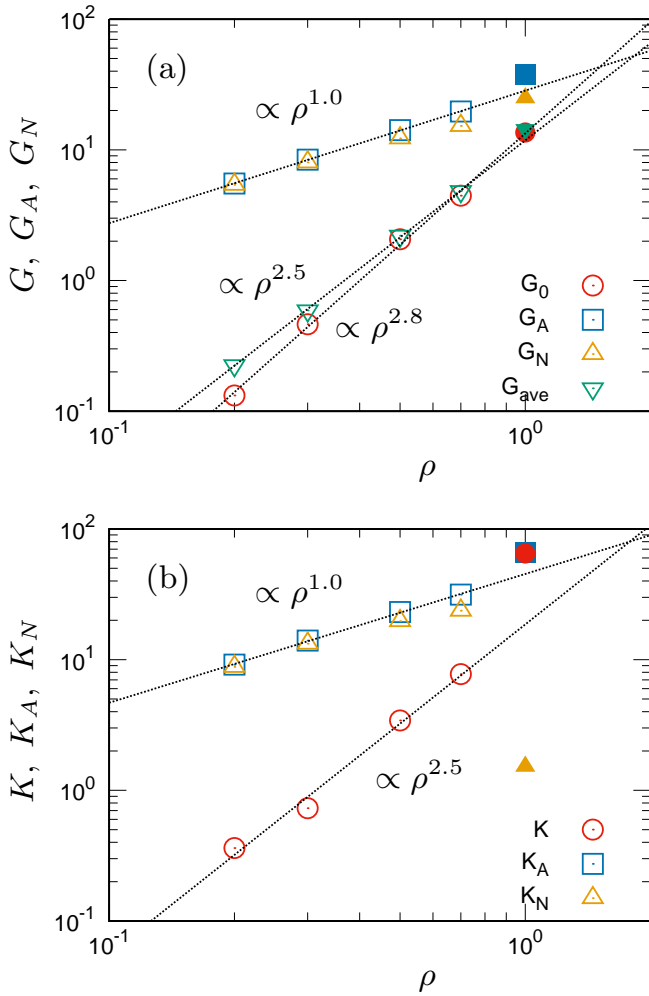


FIG. 6. Elastic moduli. (a) G and (b) K are plotted as functions of ρ . For G , two values are presented: the average value $G_{ave} = (G_1 + G_2 + G_3 + G_4 + G_5)/5$, and the minimum value $G_0 = \min(G_1, G_2, G_3, G_4, G_5)$. We also plot the affine G_A , K_A and non-affine G_N , K_N components. Note that G_A and G_N correspond to the components of G_0 . Closed symbols represent data of the glass with $\rho = 1.0$. The lines indicate power-law scalings of $G_{ave} \propto \rho^{2.5}$, $G_0 \propto \rho^{2.8}$, and $G_A, G_N \propto \rho^{1.0}$ in (a), and $K \propto \rho^{2.5}$ and $K_A, K_N \propto \rho^{1.0}$ in (b).

tence of the critical point at $\rho = 0$, where both G/G_A and K/K_A vanish and the system loses solidity, which will be discussed at the end of this paper in Sec. VI.

V. VIBRATIONAL PROPERTIES

We next present vibrational properties of the gels. We first calculated the vDOS $g(\omega)$ and then characterized each vibrational mode in terms of phonon order parameter O_k , participation ratio P_k , and vibrational energies δE_k^{\parallel} and δE_k^{\perp} . We also measured the spatial correlations $C_k(r)$ for each vibrational mode.

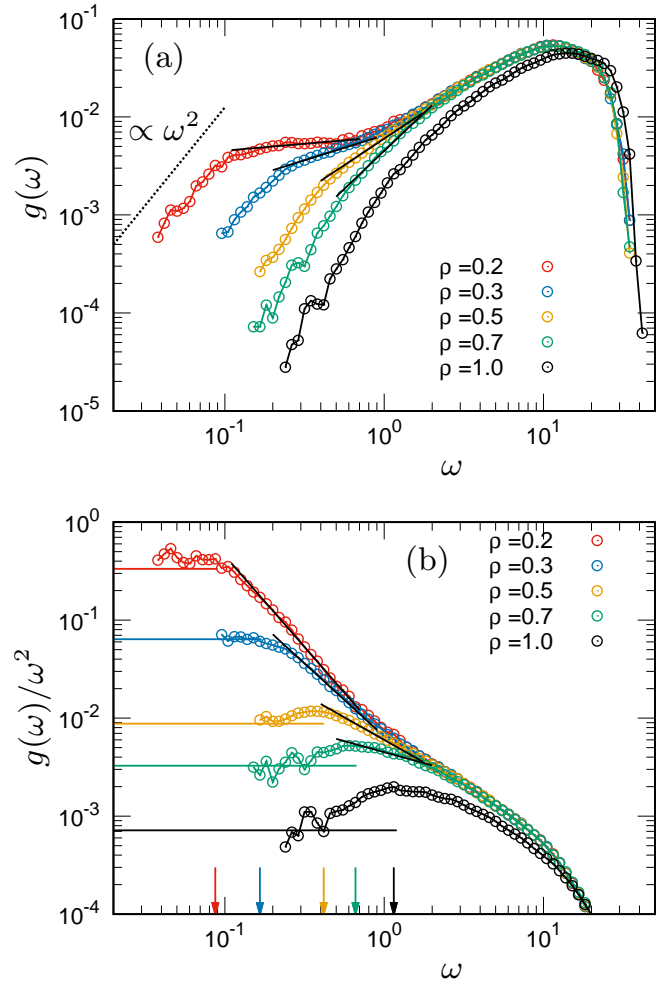


FIG. 7. Vibrational density of states. (a) $g(\omega)$ and (b) $g(\omega)/\omega^2$ are plotted as functions of ω for the densities of $\rho = 0.2, 0.3, 0.5, 0.7$ (gels) and $\rho = 1.0$ (glass). In panel (b), the horizontal lines indicate the Debye level A_D . Additionally, the arrows in (b) indicate the characteristic frequency ω_* at which $g(\omega)/\omega^2$ takes a maximum value for $\rho = 0.5, 0.7, 1.0$ or converges to A_D for $\rho = 0.2, 0.3$. Black solid lines to the data of gels with $\rho = 0.2$ to 0.7 indicate $g(\omega) \propto \omega^{\tilde{d}-1}$ with the spectral dimension \tilde{d} . Values of \tilde{d} are presented in Table I.

A. Vibrational density of states

Figure 7(a) shows the vDOS $g(\omega)$ for the densities of $\rho = 0.2, 0.3, 0.5, 0.7$ (gels) and 1.0 (glass). It is remarkable that as the density is lowered in the gels, a characteristic plateau develops in the low-frequency regime. This observation demonstrates that many low-frequency modes emerge in the gels, which form the plateau in the vDOS. With further detailed analyses, the plateau regime is characterized in terms of $g(\omega) \propto \omega^{\tilde{d}-1}$ with the spectral dimension \tilde{d} [70]. This point will be described later in Sec. VE.

In addition, we plot the reduced vDOS $g(\omega)/\omega^2$ in Fig. 7(b). In the glass with $\rho = 1.0$, we observe a clear

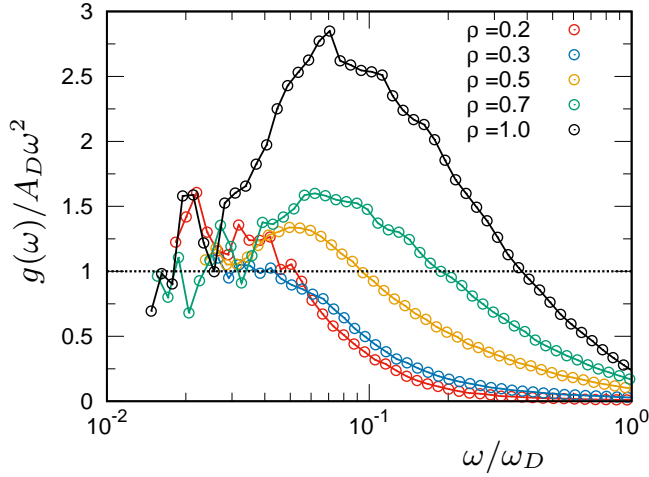


FIG. 8. Scaled vibrational density of states. $g(\omega)/A_D\omega^2$ is plotted as a function of ω/ω_D for the densities of $\rho = 0.2, 0.3, 0.5, 0.7$ (gels) and 1.0 (glass). The dotted line corresponds to the Debye vDOS $g(\omega) = A_D\omega^2$. The peak height is reduced towards 1 by lowering ρ , and no apparent peak exists at $\rho = 0.2$ and 0.3 .

peak above the Debye level A_D , which is BP [14–16]. BP is also observed in the gels with $\rho = 0.5$ and 0.7 . However, as ρ decreases, the BP is reduced, and at $\rho = 0.2$ and 0.3 , the BP disappears, so that $g(\omega)/\omega^2$ smoothly converges to A_D . We also plot $g(\omega)/(A_D\omega^2)$ in Fig. 8, where the peak height in $g(\omega)/(A_D\omega^2)$ is significantly reduced towards 1 with lowering ρ , and then no apparent peak exists at $\rho = 0.2$ and 0.3 . We can therefore conclude that the BP properties are markedly different between glasses and gels: BP is developed in glasses, whereas it is reduced and even absent in gels. In this work, we define the frequency ω_* at which $g(\omega)/\omega^2$ takes a maximum value for $\rho = 0.5, 0.7, 1.0$ or converges to A_D for $\rho = 0.2, 0.3$. The ω_* thus corresponds to the BP frequency or onset frequency of the plateau in $g(\omega)$.

B. Characterization of vibrational states

We next characterize each vibrational mode k in terms of the phonon order parameter O_k , participation ratio P_k , and vibrational energies δE_k^{\parallel} and δE_k^{\perp} , which are presented in Fig. 9. In this figure, we show data of the gel with $\rho = 0.2$ and those of the glass with $\rho = 1.0$ for comparison. Additional data for gels with $\rho = 0.3$ and 0.5 are available in Fig. S4 of SM.

Let us first examine the glass with $\rho = 1.0$ in the right panels of Fig. 9. In addition to ω_* , we define another characteristic frequency ω_G at which O_k becomes zero, $O_k \approx 0$: i.e., the character of phonon vibrations completely disappears at this frequency. In the glass, ω_* and ω_G are of the same order of magnitude, $\omega_* \sim \omega_G$. Above $\omega_* \sim \omega_G$, we observe the anomalous modes [22–24] which are disordered with $O_k \approx 0$ and extended with large P_k .

The tangential energy follows $\delta E_k^{\perp} \propto \omega_k^0$, and the normal energy $\delta E_k^{\parallel} \propto \omega_k^2$ becomes orders of magnitude larger than δE_k^{\perp} ; $\delta E_k^{\perp} \ll \delta E_k^{\parallel} \approx \delta E_k \propto \omega_k^2$. On the other hand, below $\omega_* \sim \omega_G$, phonon-like modes with large values of O_k and P_k and QLV modes with small O_k and P_k are observed. The phonon modes show $\delta E_k^{\parallel}, \delta E_k^{\perp} \propto \omega_k^2$, whereas the QLV modes follow $\delta E_k^{\parallel}, \delta E_k^{\perp} \propto \omega_k^0$. Thus, the character of the modes is qualitatively changed at $\omega_* (\sim \omega_G)$; phonon vibrations exist due to elastic-body character below ω_* , whereas above ω_* , rather disordered vibrations emerge due to structurally amorphous character. These observations of glasses were already reported in Refs. [18, 19, 60] [71].

We now turn our attention to the gel with $\rho = 0.2$ in the left panels of Fig. 9. We also visualize the vibrational states in Fig. 10 for three representative modes whose frequencies are indicated by blue arrows in panel (a) of Fig. 9. First, when examining P_k (and comparing it to that of the glass), we do not recognize the apparent existence of the QLV modes below ω_* . We find some modes with low values of P_k . However, their values of O_k are not small and $\delta E_k^{\parallel}, \delta E_k^{\perp} \propto \omega_k^2$. These observations indicate that these modes with low P_k show phonon-like vibrations that are different in nature from the QLV modes in glasses. Although QLV modes might be detected in larger system sizes, we can conclude that QLV modes are substantially suppressed or even absent in the gels.

We next examine the frequency of ω_G in the gel. Interestingly, the plateau of vDOS terminates at approximately ω_G . Above ω_G , vibrations are very similar as anomalous modes in glasses, which show $O_k \approx 0$ (disordered), large P_k (extended), and $\delta E_k^{\perp} \propto \omega_k^0 \ll \delta E_k^{\parallel} \approx \delta E_k \propto \omega_k^2$ (see also Fig. 10(c) for visualization). Note that some modes with small P_k are observed above ω_G , which will be discussed later in Sec. VF. On the other hand, below ω_G , vibrations become phonon-like with increasing O_k , and vibrational energies follow the scaling of $\delta E_k^{\parallel}, \delta E_k^{\perp} \propto \omega_k^2$ (see also Figs. 10(a) and (b) for visualization). These phonon-like modes form the characteristic plateau in the vDOS of gel at $\omega < \omega_G$.

We emphasize again that ω_* and ω_G of glasses are equivalent scales with the same order of magnitude. In contrast, in the gel with $\rho = 0.2$, these two frequencies are on different scales with different orders of magnitude, $\omega_* \ll \omega_G$. ω_* and ω_G provide the onset and end frequencies of the plateau in vDOS, respectively. As will be shown in Sec. VD and Fig. 13, these two frequencies depend on ρ differently, such that their differences become wider with lowering ρ . The character of vibrational modes is changed at these frequencies. The higher-frequency ω_G is the boundary between the elastic-body and amorphous-structure characteristics. Above ω_G , disordered vibrations emerge due to amorphous-structure character, whereas below ω_G , phonon-like vibrations associated with elastic-body character persist. The nature of the phonon vibrations below ω_G is changed at

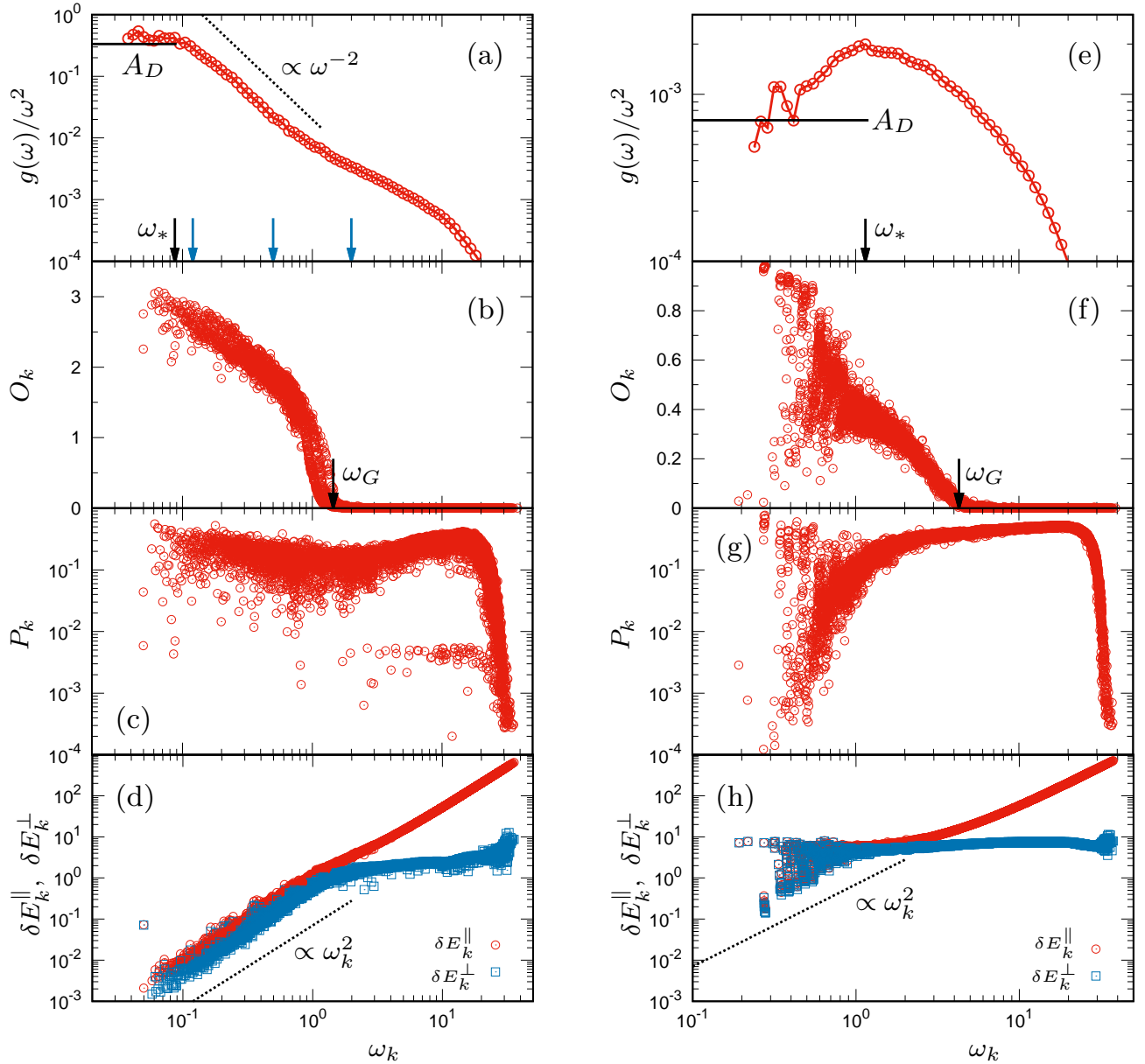


FIG. 9. Characterization of vibrational modes. Plots of (a,e) $g(\omega)/\omega^2$ and (b,f) O_k , (c,g) P_k , (d,h) δE_k^{\parallel} , and δE_k^{\perp} of each mode k as functions of ω_k . The left panels of (a) to (d) are data of the gel with $\rho = 0.2$, and the right panels of (e) to (h) are those of the glass with $\rho = 1.0$. The data of $g(\omega)/\omega^2$ are the same as those presented in Fig. 7(b). The horizontal lines in panels (a,e) present the Debye level A_D . The black arrows in (a,e) indicate the frequency ω_* , whereas those in (b,f) indicate ω_G at which O_k becomes zero, $O_k \approx 0$. The blue arrows in panel (a) indicate values of frequencies that correspond to three visualized modes in Fig. 10.

the lower-frequency ω_* ($\ll \omega_G$). The phonon vibrations above ω_* correspond to sparse, elastic bodies with heterogeneous network-like structures, whereas those below ω_* are associated with homogeneous elastic bodies. This crossover behavior at ω_* will be described next in Sec. V C.

C. Spatial correlation of displacement field

To further examine the nature of phonon-like vibrations below ω_G in the gels, we present the spatial correlation function $C_k(r)$ for modes k of $\omega_k < \omega_G$ in Fig. 11. We can see that for both the gel and the glass, $C_k(r)$ first decreases, takes a negative minimum, and then converges towards zero value with oscillation. This behavior represents typical vibrational states of transverse phonons [62], which show vortex structure, as visually recognized in

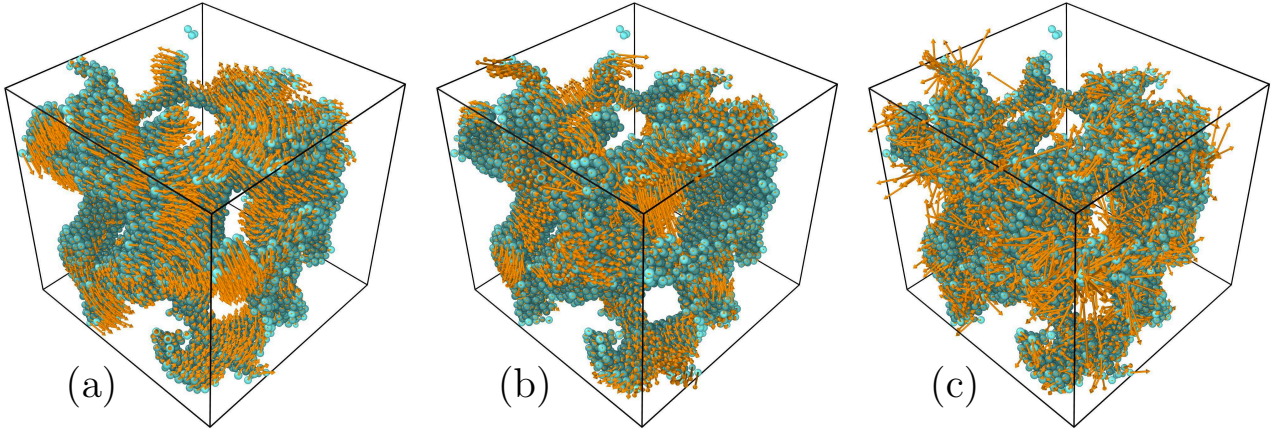


FIG. 10. Visualization of vibrational modes in the gel with $\rho = 0.2$. Vibrational states of (a) $\omega_k = 0.12$, $O_k = 2.8$, $P_k = 0.66$, (b) $\omega_k = 0.50$, $O_k = 1.9$, $P_k = 0.28$, and (c) $\omega_k = 2.0$, $O_k = 0.014$, $P_k = 0.21$ are visualized. The number of particles is $N = 10000$, and the system length is $L = 36.8$. In the figures, $200 \times \mathbf{e}_i^k$ ($i = 1, 2, \dots, N$) are plotted by arrows. Values of frequencies corresponding to three visualized modes are indicated in Fig. 9(a).

Figs. 10(a) and (b). Note that the shear modulus G_0 is smaller than half the value of the bulk modulus K in both the gels and glass, as plotted in Fig. 6. This result indicates that transverse phonon vibrations are dominant over longitudinal phonon vibrations in the low-frequency regime, which is consistent with the observations in Figs. 10 and 11. We then define the length ξ_k for each vibrational mode (of $\omega_k \leq \omega_G$) as the distance $r = \xi_k$ at which $C_k(r)$ first takes a (negative) minimum value, as indicated by closed circles in Fig. 11. ξ_k measures the length of the vortex structure, which corresponds to half of the wavelength of (transverse) phonon vibrations.

Figure 12(a) plots ξ_k versus ω_k for gels with $\rho = 0.2$ to 0.7 and glass with $\rho = 1.0$. The glass shows $\xi_k \propto \omega_k^{-1}$ dependence for the entire range of $\omega_k \leq \omega_G$. The exponent “-1” indicates the behavior of phonons propagating through homogeneous elastic media [70, 72]. As seen in Sec. III, the structure of the glass is rather homogeneous, which is consistent with the exponent “-1” and $\xi_k \propto \omega_k^{-1}$.

On the other hand, the gels show crossover behavior at some frequency $\omega_k = \omega_c$: below ω_c , $\xi_k \propto \omega_k^{-1}$ is observed, whereas $\xi_k \propto \omega_k^{-1/a}$ ($\omega_k \propto \xi_k^{-a}$) with $1/a < 1$ ($a > 1$) is observed above ω_c (see also Fig. S5 in SM). The exponent of $1/a < 1$ ($a > 1$) picks up properties of phonon vibrations in heterogeneous elastic media [70]. The value of $1/a$ decreases (a increases) with lowering of the density: $1/a = 0.88, 0.77, 0.63, 0.52$ ($a = 1.1, 1.3, 1.6, 1.9$) for $\rho = 0.7, 0.5, 0.3, 0.2$, respectively (see Fig. S5 in SM). As ρ is lowered, the structure becomes sparser and more heterogeneous, which causes the smaller value of $1/a$ (the larger value of a). We therefore conclude that the properties of phonon vibrations are changed at $\omega_k = \omega_c$: below ω_c , phonon vibrations occur through homogeneous elastic media, while above ω_c , vibrations occur in heterogeneous elastic media.

We now scale data of ξ_k versus ω_k of gels by using the length ξ_s (of static structure) and the frequency $c_T q_s = 2\pi c_T / \xi_s$, where $c_T = \sqrt{G_0 / \rho}$ is the speed of transverse phonons and $q_s = 2\pi / \xi_s$ is the characteristic wavenumber corresponding to ξ_s . Here, we employ the minimum value of shear moduli, $G_0 = \min(G_1, G_2, G_3, G_4, G_5)$, for the calculation of c_T , which is the most closely related to the low-frequency vibrations. Figure 12(b) plots $\hat{\xi}_k = \xi_k / \xi_s$ versus $\hat{\omega}_k = \omega_k / (c_T q_s) = \omega_k / (2\pi c_T / \xi_s)$. Remarkably, the crossover point at $\hat{\omega}_c = \omega_c / (c_T q_s) = \omega_c / (2\pi c_T / \xi_s)$ and data of $\hat{\omega}_k < \hat{\omega}_c$ collapse onto a single curve of $\hat{\xi}_k \propto \hat{\omega}_k^{-1}$ for different densities ρ . From the inset of Fig. 12(b), we can determine ω_c as $\omega_c \approx 0.65 c_T q_s = 1.3\pi c_T / \xi_s$. These results indicate that the crossover behavior is determined by the length ξ_s and the (transverse) phonon speed c_T or the shear modulus G_0 . For wavelengths longer than ξ_s , phonons do *not* experience sparsenesses and heterogeneities in the gels: they thus behave as if they propagate in the homogeneous media. On the other hand, for wavelengths shorter than ξ_s , phonons encounter sparsenesses and heterogeneities. We therefore conclude that phonon vibrations below ω_G are controlled by the static structural properties and the shear rigidity.

D. Characteristic frequencies

To date, we obtain three characteristic frequencies of ω_* , ω_G , and $\omega_c \approx 0.65 c_T q_s = 1.3\pi c_T / \xi_s$, which are explicitly plotted as functions of ρ in Fig. 13. For the glass with $\rho = 1.0$, ω_* and ω_G are on the same order of magnitude, as already mentioned. As the density ρ is lowered to the gel states, both frequencies decrease; however, ω_G is rather insensitive to ρ , such that the values of ω_G stay on the same order of magnitude as that of the glass ($\rho = 1.0$). In contrast, ω_* decreases significantly and becomes orders of magnitude smaller than ω_G . As a

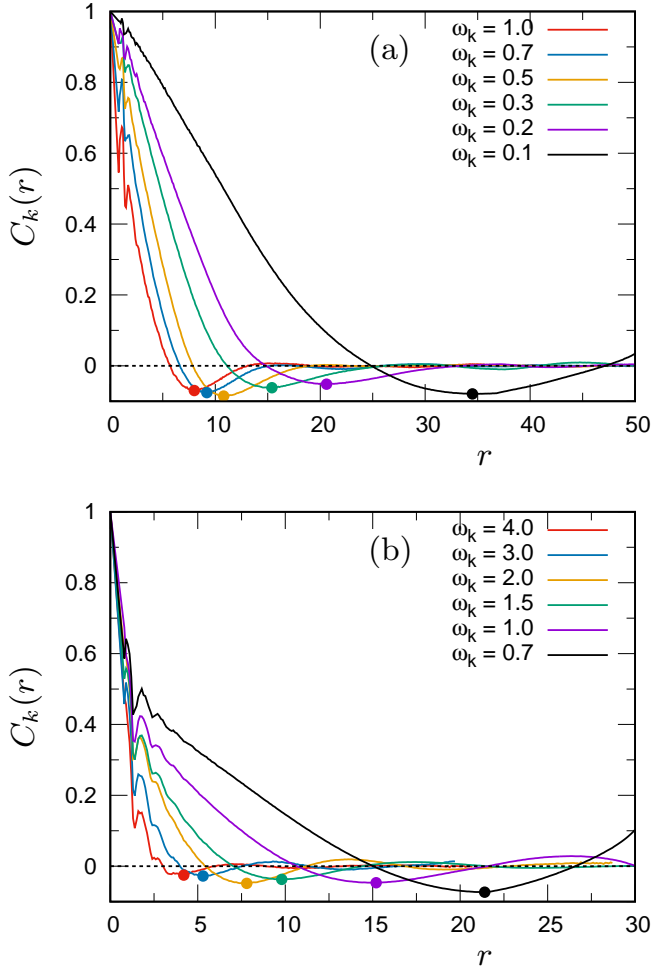


FIG. 11. Spatial correlation function for vibrational modes. $C_k(r)$ is plotted as a function of r for (a) $\rho = 0.2$ (gel) and (b) $\rho = 1.0$ (glass) and for the modes with indicated values of ω_k below ω_G . $C_k(r)$ shows nonmonotonic dependence on r , crossing the zero value of $C_k(r) = 0$ and exhibiting a negative correlation. The length ξ_k is extracted as the distance $r = \xi_k$ at which $C_k(r)$ takes a (negative) minimum value, which is indicated by closed circles.

result, ω_* and ω_G reach different scales in the gels.

Turning attention to ω_* and ω_c of the gels, it is remarkable that both frequencies depend on ρ in the same manner, as $\omega_* \approx 0.60\omega_c$. This result means that ω_* (BP frequency or onset frequency of plateau) has the same physical meaning as ω_c : below ω_* , phonon vibrations propagate through homogeneous media, whereas above ω_* , they are associated with sparse and heterogeneous media.

In addition, $\omega_* \approx 0.60\omega_c$ provides an important relationship between the frequency ω_* , the length scale in the static structure ξ_s , and the transverse sound speed c_T or the shear modulus G_0 as

$$\omega_* \approx 0.60\omega_c \approx 0.78\pi \frac{c_T}{\xi_s} \approx 0.78\pi \frac{\sqrt{G_0}}{\xi_s \sqrt{\rho}}. \quad (20)$$

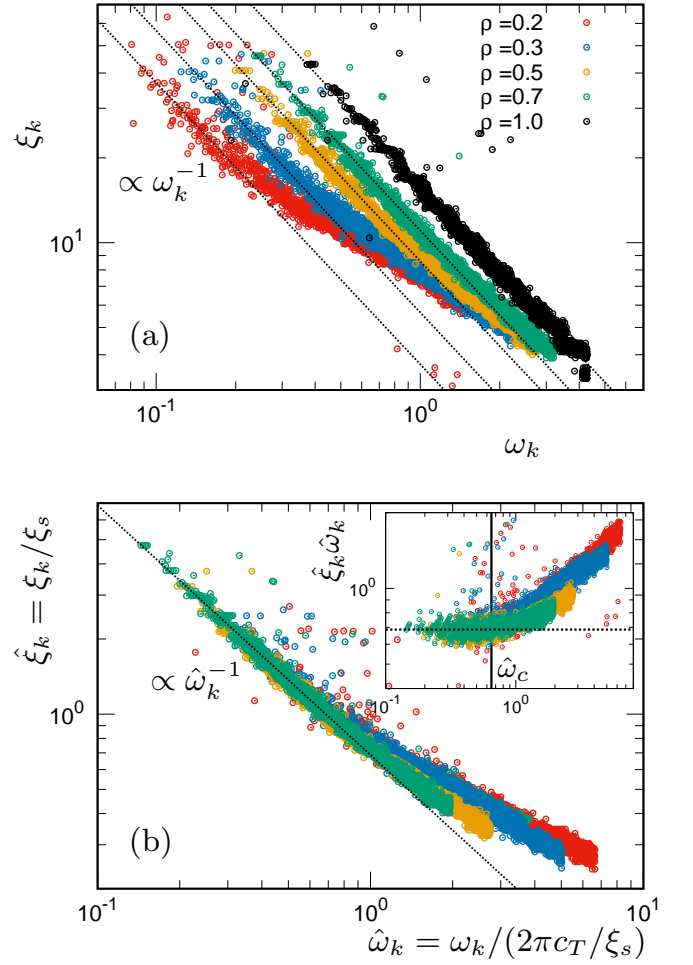


FIG. 12. Correlation length of vibrational modes. (a) ξ_k is plotted as a function of ω_k for densities of $\rho = 0.2, 0.3, 0.5, 0.7,$ and 1.0 . (b) Scaled $\xi_k = \xi_k/\xi_s$ is plotted by scaled $\hat{\omega}_k = \omega_k/(c_T q_s) = \omega_c/(2\pi c_T/\xi_s)$ (where $q_s = 2\pi/\xi_s$) for the gels with $\rho = 0.2, 0.3, 0.5,$ and 0.7 . The inset of (b) plots $\hat{\xi}_k \hat{\omega}_k$ versus $\hat{\omega}_k$. The lines indicate $\propto \omega_k^{-1}$ in (a) and $\propto \hat{\omega}_k^{-1}$ in (b). $\hat{\xi}_k \propto \hat{\omega}_k^{-1}$ collapses for different densities below the crossover frequency of $\hat{\omega}_c = \omega_c/(c_T q_s) = \omega_c/(2\pi c_T/\xi_s)$. From the inset of (b), we obtain $\omega_c = 0.65c_T q_s = 1.3\pi c_T/\xi_s$.

Substituting the scalings of $\xi_s \propto \rho^{-0.7}$ [in Eq. (17) and Fig. 4] and $G_0 \propto \rho^{2.8}$ [in Eq. (18) and Fig. 6] into ω_* in Eq. (20), we obtain

$$\omega_* \propto \omega_c \propto \rho^{1.6}, \quad (21)$$

which is indeed consistent with the observation of Fig. 13. From Eq. (20), we can conclude that the onset regime of the plateau is composed of phonon-like modes with wavelengths comparable to the length scale of the heterogeneous structure.

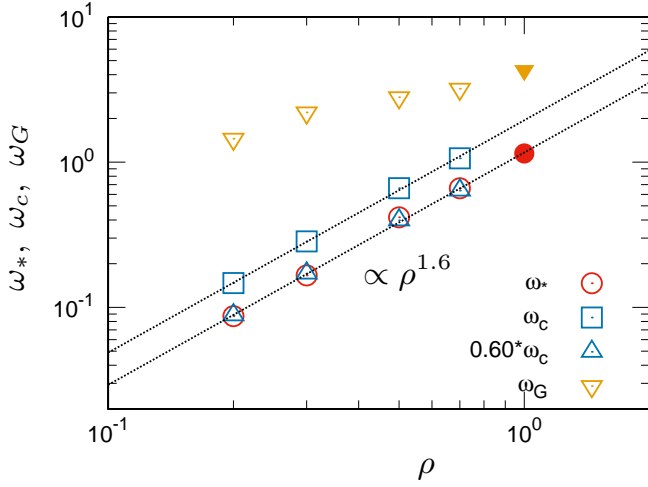


FIG. 13. Characteristic frequencies. ω_* , ω_c ($= 0.65c_T q_s = 1.3\pi c_T / \xi_s$), and ω_G are plotted as functions of ρ . Closed symbols represent data of the glass with $\rho = 1.0$. $\omega_* \approx 0.60\omega_c$ is observed for the gels with $\rho = 0.2$ to 0.7 . The lines demonstrate $\omega_* \approx 0.60\omega_c \approx 0.78\pi c_T / \xi_s \propto \rho^{1.6}$.

TABLE I. Summary of values of fractal dimension D_f , exponent a of dispersion curve, and spectral dimension \tilde{d} in the gel states of $\rho = 0.2$ to 0.7 .

| ρ | 0.2 | 0.3 | 0.5 | 0.7 | Def. | Ref. |
|---------------------|-----|-----|-----|-----|--|---------------|
| D_f | 2.2 | 2.4 | 2.7 | 2.9 | $N(r) \propto r^{D_f}$ | Fig. S2 of SM |
| a | 1.9 | 1.6 | 1.3 | 1.1 | $\omega_k \propto \xi_k^{-a}$ | Fig. S5 of SM |
| $\tilde{d} = D_f/a$ | 1.1 | 1.5 | 2.1 | 2.6 | $g(\omega) \propto \omega^{\tilde{d}-1}$ | Fig. 7 |

E. Spectral dimension of vDOS

Here, we discuss the spectral dimension of vDOS for the gel states of $\rho = 0.2$ to 0.7 . In Sec. III C and Figs. 3 and S2 of SM, we have obtained

$$N(r) \begin{cases} \propto r^3 (= r^d) & (r > \xi_s), \\ \propto r^{D_f} & (r < \xi_s), \end{cases} \quad (22)$$

which indicates the existence of a fractal-like structure with fractal dimension $D_f < 3$ at $r < \xi_s$. In addition, in Sec. V C and Figs. 12 and S5 of SM, we have shown

$$\omega_k \begin{cases} \propto \xi_k^{-1} & (\xi_k > \xi_s \ \& \ \omega_k < \omega_c), \\ \propto \xi_k^{-a} & (\xi_k < \xi_s \ \& \ \omega_c < \omega_k < \omega_G), \end{cases} \quad (23)$$

which provides the dispersion relation with the exponent of $a > 1$ for the phonon-like vibrations of $\xi_k < \xi_s$. By using the information of Eqs. (22) and (23), we can predict the behavior of vDOS [70] as

$$g(\omega) \begin{cases} \propto \omega^2 (= \omega^{d-1}) & (\omega < \omega_* \sim \omega_c), \\ \propto \omega^{D_f/a-1} = \omega^{\tilde{d}-1} & (\omega_* \sim \omega_c < \omega < \omega_G), \end{cases} \quad (24)$$

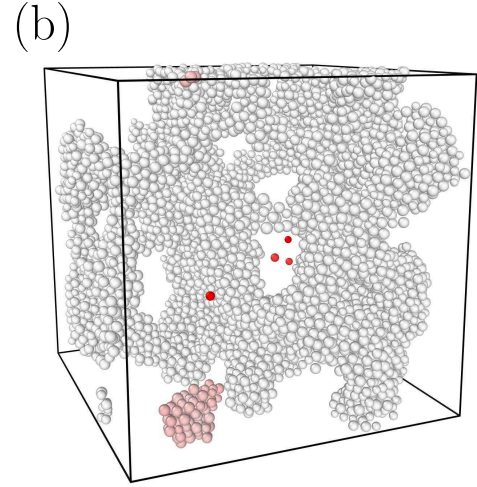
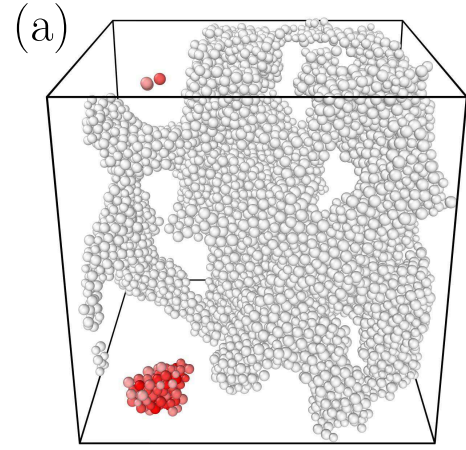


FIG. 14. Isolated vibrational states in the gel with $\rho = 0.2$. (a) Isolated vibrations with finite frequency $\omega_k > \omega_G$ and (b) those with zero frequency $\omega_k = 0$ ($\omega_k < 10^{-5}$). In (a), for each particle i , we plot by red color summation of $|\mathbf{e}_i^k|$ over the modes with $\omega_k > \omega_G$ and $P_k < 10^{-2}$; $d_i = \sum_{k; \omega_k > \omega_G \ \& \ P_k < 10^{-2}} |\mathbf{e}_i^k|$. In (b), we plot $d'_i = \sum_{k; \omega_k < 10^{-5}} |\mathbf{e}_i^k|$. White color means zero value, while red color means finite d_i or d'_i . The number of particles is $N = 10000$. Only particles in an isolated cluster and isolated particles participate in these two vibrational states (a) and (b), with finite displacements.

where $\tilde{d} = D_f/a$ is called the spectral dimension. Note that for the case of $r > \xi_s$ and $\omega < \omega_*$, D_f and a correspond to $D_f = d = 3$ and $a = 1$, which gives $\tilde{d} = d = 3$, i.e., the Debye scaling behavior.

We summarize the values of D_f , a , and $\tilde{d} = D_f/a$ in Table I. Figure 7 plots by black lines the scaling of $g(\omega) \propto \omega^{\tilde{d}-1}$ in the plateau regime of $\omega_* < \omega < \omega_G$, which indeed confirms the validity of Eq. (24) and the values of the spectral dimension $\tilde{d} = D_f/a$. We can therefore understand the plateau of vDOS of gels in terms of the spectral dimension.

F. Isolated vibrational states

Finally, we note that localized vibrational modes exist with small values of $P^k < 10^{-2}$ and relatively high frequencies $\omega_k > \omega_G$ in the gel with $\rho = 0.2$, as recognized in panel (c) of Fig. 9. To understand these modes, we calculate for each particle i the summation of $|\mathbf{e}_i^k|$ over $\omega_k > \omega_G$ and $P_k < 10^{-2}$; $d_i = \sum_{k; \omega_k > \omega_G \ \& \ P_k < 10^{-2}} |\mathbf{e}_i^k|$. Figure 14(a) plots by red color the spatial distribution of d_i in the gel with $\rho = 0.2$ and $N = 10000$. From the figure, we clearly recognize that all of the vibrating particles (red particles) belong to a cluster that is isolated from the network structure, whereas the other particles do not at all participate in vibrations. We therefore conclude that localized vibrations of $\omega_k > \omega_G$ are due to clusters isolated from the network structure of the gels.

In addition, as we also note in Sec. II C, there are several modes with zero frequency $\omega_k = 0$ ($\omega_k < 10^{-5}$) in the gels with $\rho = 0.2$ and 0.3 . Similarly, for these zero modes, we calculate $d'_i = \sum_{k; \omega_k < 10^{-5}} |\mathbf{e}_i^k|$ for each particle i and plot the spatial distribution of d'_i in Fig. 14(b). It is clear that zero modes originate from an isolated cluster of particles and isolated particles. We therefore naturally conclude that isolated clusters and particles produce zero-frequency modes in the gel states.

VI. DISCUSSION AND CONCLUSIONS

In summary, we have studied the simplest model of particulate physical gels (and glass) composed of LJ particles at zero temperature and have provided a comprehensive understanding of their structural, mechanical, and vibrational properties.

- (1) The gels show a sparse, heterogeneous, network-like structure, where clusters of glasses are connected to form the fractal structure of fractal dimension $2 < D_f < 3$. As the density is lowered, the structure becomes sparser and more heterogeneous, which is captured by a growing characteristic length scale ξ_s .
- (2) Both the shear G and bulk K moduli of the gels significantly decrease with decreasing density. The gels can become extremely soft, with elastic moduli orders of magnitude smaller than those of glasses. In particular, the gels undergo the non-affine deformation even under isotropic bulk deformation and show rather small value of the bulk modulus.
- (3) Many low-frequency vibrational modes emerge, which form the characteristic plateau in the vDOS. The vibrational states are changed at the onset frequency ω_* and the end frequency ω_G of the plateau ($\omega_* \ll \omega_G$). At higher ω_G , there is crossover between the phonon vibrations due to the elastic body at $\omega < \omega_G$ and the disordered vibrations due to the amorphous structure at $\omega > \omega_G$. At $\omega < \omega_G$, the vibrations are phonon-like, showing crossover at

the lower ω_* between those associated with a homogeneous elastic body at $\omega < \omega_*$ and those associated with a heterogeneous elastic body at $\omega > \omega_*$.

- (4) In the plateau regime of $\omega_* < \omega < \omega_G$, the fractal structure with D_f plays an important role in the vibrational states. The dispersion curve is described as $\omega_k \propto \xi_k^{-a}$ with $a > 1$, which gives the vDOS $g(\omega) \propto \omega^{\tilde{d}-1}$ with the spectral dimension $\tilde{d} = D_f/a$.
- (5) Compared to the glasses, the BP is reduced and even absent in the gels, such that the vDOS smoothly converges to the Debye behavior at low frequencies below ω_* . Also, the QLV modes are suppressed in the gels. These properties of BP and QLVs markedly contrast with those of glasses.
- (6) The abovementioned characteristic quantities show power-law dependences on the density ρ , such as $\xi_s \propto \rho^{-0.7}$, $G_0 \propto \rho^{2.8}$, and $\omega_* \propto \rho^{1.6}$. These power-law scalings are closely related via $\omega_* \propto c_T/\xi_s \propto \sqrt{G_0/\rho}/\xi_s$, which establishes the relationship of structural, mechanical, and vibrational properties of the gels.

In glasses, there is a characteristic frequency (BP frequency) $\omega_* \sim \omega_G$ and associated length scale $\xi_* \propto c_T/\omega_*$ (or $\omega_* \propto c_T/\xi_*$) [11]. ω_* and ξ_* are the crossover points between the elastic body and the amorphous structural body. Note that ξ_* can be extracted from the elastic response to local deformation [11, 73, 74] and global deformation [75, 76] or phonon transport properties [77–79]. In contrast to the glasses, the gels exhibit two characteristic frequencies, ω_* and ω_G . In the gels, the growing length ξ_s of the static structure controls the ω_* as $\omega_* \propto c_T/\xi_s$ and separates two frequencies as $\omega_* \ll \omega_G$. Note that the length $\xi_G \propto c_T/\omega_G$ (or $\omega_G \propto c_T/\xi_G$) (which corresponds to ξ_* in the glasses) also exists in the gels, and since $\omega_G \gg \omega_*$, it is much smaller than ξ_s , $\xi_G \ll \xi_s$. We therefore conclude that the present gels are multiscale, solid-state materials: (i) homogeneous elastic bodies at long lengths above ξ_s and low frequencies below ω_* , (ii) heterogeneous elastic bodies with fractal structures at intermediate lengths between ξ_s and ξ_G and frequencies between ω_* and ω_G , and (iii) amorphous structural bodies at short lengths below ξ_G and high frequencies above ω_G .

In addition, it is remarkable that BP and QLVs are suppressed and even absent in the gels, which is a markedly contrasting situation with respect to glasses. In glasses, repulsions are dominant between particle interactions, whereas attractive interactions play an important role in constructing network structures in gels [6, 80]. It has been reported that in glasses, the strength of the BP and number of QLVs decrease with weakening repulsive interactions or strengthening attractive interactions between particles [81–83]. From these observations, we speculate that in the gels, attractive forces may play a role in suppressing BP and QLVs. This point should be clarified in detail in the future.

We note that the present gels can be considered porous glasses or aerogels such as silicate gels. The most recent work [84] in the context of porous glasses studied the mechanical properties of systems similar to the present ones. They obtained density dependences of elastic moduli that are the same as those in Eq. (18), and found scaling with the porosity that can be explained in a semi-empirical way [85]. Also, the recent simulations [86, 87] demonstrated scalings with volume fraction in the jammed solids of sticky particles, where both the shear and bulk moduli vanish at the sticky jamming transition point. In addition, a previous series of works [88–92] performed scattering experiments, such as Brillouin, Raman, and inelastic neutron scattering, on silica aerogels and measured the vDOS (and dispersion curve and line-width for acoustic excitations). The characteristic plateau in the vDOS and crossover to the Debye behavior were observed, which are completely consistent with our simulation results. This work also characterized vibrational modes in the plateau regime in terms of so-called fractons, which are highly localized vibrations on the fractal structure [53, 70, 93]. Further investigations are necessary to understand the relevance of our phonon vibrations to the heterogeneous structure with the fractons.

We also note that network-type glasses such as silicate glasses [94] and glasses close to the jamming transition [27] also show a plateau in the vDOS. The plateau in these systems is understood to originate from an isotropic nature [22–24], which is a different mechanism versus the case of gels, where the development of the plateau is simply associated with a reduction in global elastic moduli. The scaled vDOS $g(\omega)/A_D\omega^2$ and BP diverge in glasses approaching the jamming transition [18], whereas $g(\omega)/A_D\omega^2$ smoothly converges to 1 in the gels (as explicitly plotted in Fig. 8). In addition, vibrational modes in the plateaus are markedly different in nature between these glassy systems and the gels: they are anomalous modes with disordered vibrations in the glasses [18, 21], whereas those in the gels show phonon-like vibrations.

Finally, we discuss the critical-like behaviors observed in the present particulate gels. We found power-law scalings with density ρ in the structure, elastic moduli, and vibrational states as $\xi_s \propto \rho^{-0.7}$, $G_0 \propto \rho^{2.8}$, $G_{ave} \propto K \propto \rho^{2.5}$ (or $G_0/G_A \propto \rho^{1.8}$, $G_{ave}/G_A \propto K/K_A \propto \rho^{1.5}$), and $\omega_* \propto \rho^{1.6}$. This observation implies the existence of a critical phenomenon with the critical point at $\rho = 0$, where the length diverges, elastic moduli vanish, and the frequency goes to zero. Note that our simulations show that the network structure breaks down at a density of $\rho = 0.1$. In this work, we set the cut-off distance of the potential to be finite as $r_c = 3.0$, which can result in the breakdown of the network. We speculate that if r_c is set to infinity, the gels retain the network structures as $\rho \rightarrow 0$, and the power-law scalings persist down to $\rho = 0$. Previous experiments also reported scaling behaviors in the elastic moduli [32–35] and the vibrational and acoustic properties [88–92]. These power-law scalings are consistent with predictions of rigidity percolation theory [95–97]. Note that the theory provides different values of critical points and exponents depending on the details of the models [98–101]. Additionally, the jamming transition of glassy systems is well understood by using the mean-field approximation theory of rigidity percolation [102–104]. Further studies are necessary to understand the properties around the critical point of the gels.

ACKNOWLEDGMENTS

This work was supported by JSPS KAKENHI Grant Numbers 18H05225, 19K14670, 19H01812, 20H01868, and 20H00128.

DATA AVAILABILITY

The data that supports the findings of this study are available within the article and its supplementary material.

-
- [1] W. A. Phillips, *Amorphous Solids: Low Temperature Properties*, 3rd ed. (Springer, Berlin, 1981).
 - [2] L. Berthier and G. Biroli, *Rev. Mod. Phys.* **83**, 587 (2011).
 - [3] R. Larson, *The Structure and Rheology of Complex Fluids*, Topics in Chemical Engineering (OUP USA, 1999).
 - [4] P. Flory, *Principles of Polymer Chemistry*, Baker lectures 1948 (Cornell University Press, 1953).
 - [5] P. de Gennes, *Scaling Concepts in Polymer Physics* (Cornell University Press, 1979).
 - [6] E. Zaccarelli, *Journal of Physics: Condensed Matter* **19**, 3231 (2007).
 - [7] J. Mewis and N. Wagner, *Colloidal Suspension Rheology*, Cambridge Series in Chemical Engineering (Cambridge University Press, 2012).
 - [8] P. J. Lu and D. A. Weitz, *Annual Review of Condensed Matter Physics* **4**, 217 (2013).
 - [9] J. Ruiz-Franco and E. Zaccarelli, *Annual Review of Condensed Matter Physics* **12**, 51 (2021).
 - [10] A. Tanguy, J. P. Wittmer, F. Leonforte, and J.-L. Barrat, *Phys. Rev. B* **66**, 174205 (2002).
 - [11] F. Leonforte, R. Boissière, A. Tanguy, J. P. Wittmer, and J.-L. Barrat, *Phys. Rev. B* **72**, 224206 (2005).
 - [12] A. Zaccone and E. Scossa-Romano, *Phys. Rev. B* **83**, 184205 (2011).
 - [13] Mizuno, S. Mossa, and J.-L. Barrat, *Phys. Rev. E* **87**, 042306 (2013).
 - [14] U. Buchenau, N. Nücker, and A. J. Dianoux, *Phys. Rev. Lett.* **53**, 2316 (1984).

- [15] O. Yamamuro, T. Matsuo, K. Takeda, T. Kanaya, T. Kawaguchi, and K. Kaji, *The Journal of Chemical Physics* **105**, 732 (1996).
- [16] T. Mori, Y. Jiang, Y. Fujii, S. Kitani, H. Mizuno, A. Koreeda, L. Motoji, H. Tokoro, K. Shiraki, Y. Yamamoto, and S. Kojima, *Phys. Rev. E* **102**, 022502 (2020).
- [17] E. Lerner, G. Düring, and E. Bouchbinder, *Phys. Rev. Lett.* **117**, 035501 (2016).
- [18] H. Mizuno, H. Shiba, and A. Ikeda, *Proceedings of the National Academy of Sciences* **114**, E9767 (2017).
- [19] M. Shimada, H. Mizuno, and A. Ikeda, *Phys. Rev. E* **97**, 022609 (2018).
- [20] L. Wang, A. Ninarello, P. Guan, L. Berthier, G. Szamel, and E. Flenner, *Nature Communications* **10**, 26 (2019).
- [21] L. E. Silbert, A. J. Liu, and S. R. Nagel, *Phys. Rev. E* **79**, 021308 (2009).
- [22] M. Wyart, S. R. Nagel, and T. A. Witten, *EPL (Europhysics Letters)* **72**, 486 (2005).
- [23] M. Wyart, L. E. Silbert, S. R. Nagel, and T. A. Witten, *Phys. Rev. E* **72**, 051306 (2005).
- [24] M. Wyart, *Annales de Physiques* **30**, 1 (2005).
- [25] C. S. O'Hern, L. E. Silbert, A. J. Liu, and S. R. Nagel, *Phys. Rev. E* **68**, 011306 (2003).
- [26] M. van Hecke, *Journal of Physics: Condensed Matter* **22**, 033602 (2010).
- [27] L. E. Silbert, A. J. Liu, and S. R. Nagel, *Phys. Rev. Lett.* **95**, 098301 (2005).
- [28] A. Fernandez-Nieves and A. Puertas, *Fluids, Colloids and Soft Materials: An Introduction to Soft Matter Physics*, Wiley Series on Surface and Interfacial Chemistry (Wiley, 2016).
- [29] T. A. Witten and L. M. Sander, *Phys. Rev. B* **27**, 5686 (1983).
- [30] D. A. Weitz, J. S. Huang, M. Y. Lin, and J. Sung, *Phys. Rev. Lett.* **54**, 1416 (1985).
- [31] M. Carpineti and M. Giglio, *Phys. Rev. Lett.* **68**, 3327 (1992).
- [32] M. C. Grant and W. B. Russel, *Phys. Rev. E* **47**, 2606 (1993).
- [33] A. H. Krall and D. A. Weitz, *Phys. Rev. Lett.* **80**, 778 (1998).
- [34] V. Trappe and D. A. Weitz, *Phys. Rev. Lett.* **85**, 449 (2000).
- [35] V. Prasad, V. Trappe, A. D. Dinsmore, P. N. Segre, L. Cipelletti, and D. A. Weitz, *Faraday Discuss.* **123**, 1 (2003).
- [36] R. Yamamoto and K. Nakanishi, *Phys. Rev. B* **49**, 14958 (1994).
- [37] A. E. Bailey, W. C. K. Poon, R. J. Christianson, A. B. Schofield, U. Gasser, V. Prasad, S. Manley, P. N. Segre, L. Cipelletti, W. V. Meyer, M. P. Doherty, S. Sankaran, A. L. Jankovsky, W. L. Shiley, J. P. Bowen, J. C. Eggers, C. Kurta, T. Lorik, P. N. Pusey, and D. A. Weitz, *Phys. Rev. Lett.* **99**, 205701 (2007).
- [38] P. J. Lu, E. Zaccarelli, F. Ciulla, A. B. Schofield, F. Sciortino, and D. A. Weitz, *Nature* **453**, 499 (2008).
- [39] V. Testard, L. Berthier, and W. Kob, *Phys. Rev. Lett.* **106**, 125702 (2011).
- [40] V. Testard, L. Berthier, and W. Kob, *The Journal of Chemical Physics* **140**, 164502 (2014).
- [41] M. Tateno and H. Tanaka, *Nature Communications* **12**, 912 (2021).
- [42] Y. Oku, K. Takae, and A. Ikeda, "Phase separation kinetics of a symmetric binary mixture of glass-forming liquids," (2020), arXiv:2004.02103 [cond-mat.stat-mech].
- [43] V. Trappe, V. Prasad, L. Cipelletti, P. N. Segre, and D. A. Weitz, *Nature* **411**, 772 (2008).
- [44] A. Zaccone, H. Wu, and E. Del Gado, *Phys. Rev. Lett.* **103**, 208301 (2009).
- [45] A. Zaccone, H. H. Winter, M. Siebenbürger, and M. Ballauff, *Journal of Rheology* **58**, 1219 (2014).
- [46] C. Patrick Royall, S. R. Williams, T. Ohtsuka, and H. Tanaka, *Nature Materials* **7**, 556 (2008).
- [47] L. C. Hsiao, R. S. Newman, S. C. Glotzer, and M. J. Solomon, *Proceedings of the National Academy of Sciences* **109**, 16029 (2012).
- [48] H. Tsurusawa, M. Leocmach, J. Russo, and H. Tanaka, *Science Advances* **5** (2019), 10.1126/sciadv.aav6090.
- [49] N. E. Valadez-Pérez, Y. Liu, A. P. R. Eberle, N. J. Wagner, and R. Castañeda Priego, *Phys. Rev. E* **88**, 060302 (2013).
- [50] S. Zhang, L. Zhang, M. Bouzid, D. Z. Rocklin, E. Del Gado, and X. Mao, *Phys. Rev. Lett.* **123**, 058001 (2019).
- [51] W. Press, B. Flannery, S. Teukolsky, W. Vetterling, and B. Flannery, *Numerical Recipes: The Art of Scientific Computing*, 3rd ed. (Cambridge University Press, New York, 2007).
- [52] J. Hansen and I. R. McDonald, *Theory of Simple Liquids*, 3rd ed. (Academic, London, 2006).
- [53] D. Stauffer and A. Aharony, *Introduction to Percolation Theory*, 2nd ed. (Taylor and Francis, Oxford, 1992).
- [54] G. Leibfried and N. Breuer, *Point Defects in Metals I, Introduction to the Theory*, Springer Tracts in Modern Physics, Vol. 81 (Springer, Berlin, 1978).
- [55] H. Mizuno and A. Ikeda, "Computational simulations of the vibrational properties of glasses," (2021), arXiv:2101.01371 [cond-mat.soft].
- [56] The largest system size N_{\max} used in the vibrational mode analysis depends on the density ρ ; $N_{\max} = 640000$ for $\rho = 1.0$ and 0.7 , 320000 for $\rho = 0.5$, 160000 for $\rho = 0.3$, and 80000 for $\rho = 0.2$.
- [57] H. R. Schober and B. B. Laird, *Phys. Rev. B* **44**, 6746 (1991).
- [58] V. Mazzacurati, G. Ruocco, and M. Sampoli, *Europhys. Lett.* **34**, 681 (1996).
- [59] S. N. Taraskin and S. R. Elliott, *Phys. Rev. B* **59**, 8572 (1999).
- [60] H. Mizuno, K. Saitoh, and L. E. Silbert, *Phys. Rev. E* **93**, 062905 (2016).
- [61] M. Shimada, H. Mizuno, M. Wyart, and A. Ikeda, *Phys. Rev. E* **98**, 060901 (2018).
- [62] H. Mizuno, L. E. Silbert, M. Sperl, S. Mossa, and J.-L. Barrat, *Phys. Rev. E* **93**, 043314 (2016).
- [63] J. F. Lutsko, *J. Appl. Phys.* **65**, 2991 (1989).
- [64] A. Lemaitre and C. Maloney, *Journal of Statistical Physics* **123**, 415 (2006).
- [65] Y. Asano and K. Fuchizaki, *The Journal of Chemical Physics* **137**, 174502 (2012).
- [66] S. Sastry, *Phys. Rev. Lett.* **85**, 590 (2000).
- [67] Y. E. Altabet, F. H. Stillinger, and P. G. Debenedetti, *The Journal of Chemical Physics* **145**, 211905 (2016).
- [68] M. Shimada and N. Oyama, arXiv:2011.12489 (2020).
- [69] A. Bray, *Advances in Physics* **43**, 357 (1994).
- [70] T. Nakayama, K. Yakubo, and R. L. Orbach, *Rev. Mod. Phys.* **66**, 381 (1994).
- [71] In Ref. [18], we denote ω_* (the BP frequency) as ω_{BP} , while in this paper it is denoted as ω_* .

- [72] N. W. Ashcroft and N. D. Mermin, *Solid State Physics* (Harcourt College Publishers, New York, 1976).
- [73] W. G. Ellenbroek, M. van Hecke, and W. van Saarloos, *Phys. Rev. E* **80**, 061307 (2009).
- [74] E. Lerner, E. DeGiuli, G. During, and M. Wyart, *Soft Matter* **10**, 5085 (2014).
- [75] K. Karimi and C. E. Maloney, *Phys. Rev. E* **92**, 022208 (2015).
- [76] H. Mizuno and S. Mossa, *Condensed Matter Physics* **22**, 43604 (2019).
- [77] H. Mizuno and A. Ikeda, *Phys. Rev. E* **98**, 062612 (2018).
- [78] A. Moriel, G. Kapteijns, C. Rainone, J. Zylberg, E. Lerner, and E. Bouchbinder, *The Journal of Chemical Physics* **151**, 104503 (2019).
- [79] L. Wang, L. Berthier, E. Flenner, P. Guan, and G. Szamel, *Soft Matter* **15**, 7018 (2019).
- [80] H. Tanaka, J. Meunier, and D. Bonn, *Phys. Rev. E* **69**, 031404 (2004).
- [81] N. Xu, M. Wyart, A. J. Liu, and S. R. Nagel, *Phys. Rev. Lett.* **98**, 175502 (2007).
- [82] E. Lerner and E. Bouchbinder, *Phys. Rev. E* **97**, 032140 (2018).
- [83] K. González-López, M. Shivam, Y. Zheng, M. P. Ciamarra, and E. Lerner, *Phys. Rev. E* **103**, 022605 (2021).
- [84] S. Niyogi and B. S. Gupta, “Mechanical properties and pore size distribution in athermal shear-strained porous glasses,” (2021), arXiv:2106.03473 [cond-mat.soft].
- [85] K. K. Phani and S. K. Niyogi, *Journal of Materials Science* **22**, 257 (1987).
- [86] D. J. Koeze and B. P. Tighe, *Phys. Rev. Lett.* **121**, 188002 (2018).
- [87] D. J. Koeze, L. Hong, A. Kumar, and B. P. Tighe, *Phys. Rev. Research* **2**, 032047 (2020).
- [88] E. Courtens, J. Pelous, J. Phalippou, R. Vacher, and T. Woignier, *Phys. Rev. Lett.* **58**, 128 (1987).
- [89] E. Courtens, R. Vacher, J. Pelous, and T. Woignier, *Europhysics Letters (EPL)* **6**, 245 (1988).
- [90] R. Vacher and E. Courtens, *Physica Scripta* **T29**, 239 (1989).
- [91] R. Vacher, E. Courtens, G. Coddens, A. Heidemann, Y. Tsujimi, J. Pelous, and M. Foret, *Phys. Rev. Lett.* **65**, 1008 (1990).
- [92] E. Anglaret, A. Hasmy, E. Courtens, J. Pelous, and R. Vacher, *Europhysics Letters (EPL)* **28**, 591 (1994).
- [93] S. Alexander, *Phys. Rev. B* **40**, 7953 (1989).
- [94] K. Trachenko, M. Dove, M. Harris, and V. Heine, *Journal of Physics: Condensed Matter* **12**, 8041 (2000).
- [95] S. Feng and P. N. Sen, *Phys. Rev. Lett.* **52**, 216 (1984).
- [96] Y. Kantor and I. Webman, *Phys. Rev. Lett.* **52**, 1891 (1984).
- [97] S. Feng, *Phys. Rev. B* **32**, 5793 (1985).
- [98] S. Feng, *Phys. Rev. B* **32**, 510 (1985).
- [99] B. I. Halperin, S. Feng, and P. N. Sen, *Phys. Rev. Lett.* **54**, 2391 (1985).
- [100] S. Arbabi and M. Sahimi, *Phys. Rev. B* **47**, 695 (1993).
- [101] M. Sahimi and S. Arbabi, *Phys. Rev. B* **47**, 703 (1993).
- [102] S. Feng, M. F. Thorpe, and E. Garboczi, *Phys. Rev. B* **31**, 276 (1985).
- [103] M. Wyart, *EPL (Europhysics Letters)* **89**, 64001 (2010).
- [104] E. DeGiuli, A. Laversanne-Finot, G. During, E. Lerner, and M. Wyart, *Soft Matter* **10**, 5628 (2014).

SUPPLEMENTARY MATERIAL

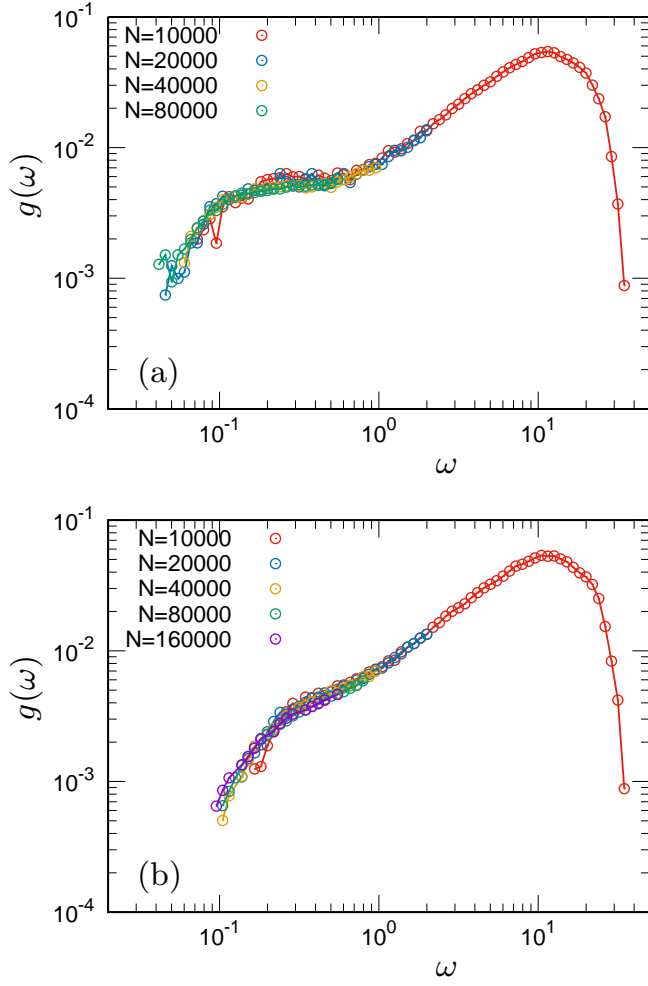


FIG. S1. Vibrational density of states from different system sizes. $g(\omega)$ is plotted as a function of ω for different system sizes of $N = 10000$ to 160000 . The density is (a) $\rho = 0.2$ and (b) 0.3 . Data from different system sizes are smoothly connected as a function of ω .

We report supplementary data, including the vDOS from different system sizes (Fig. S1), fractal dimension D_f of $N(r) \propto r^{D_f}$ (Fig. S2), five components of shear moduli (Fig. S3), data of characterization of each vibrational mode for the gels with $\rho = 0.3$ and 0.5 (Fig. S4), and exponent $1/a$ of $\xi_k \propto \omega_k^{-1/a}$ (Fig. S5).

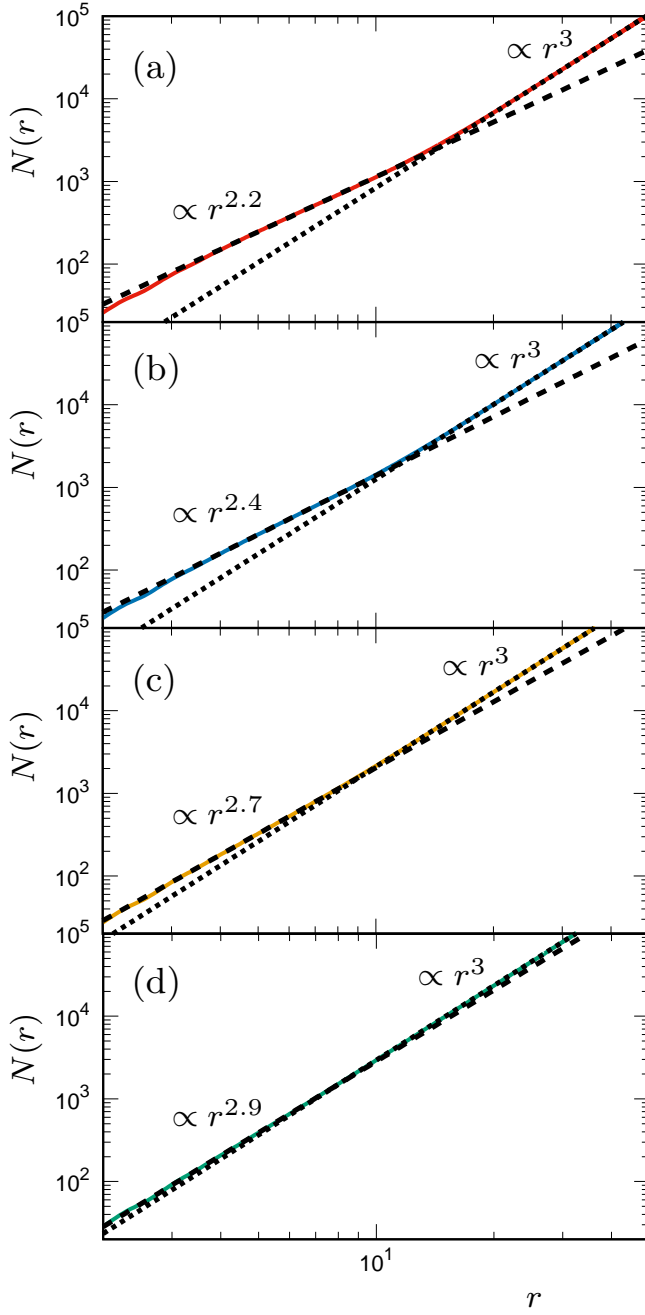


FIG. S2. Fractal dimension D_f of $N(r) \propto r^{D_f}$ (at $r < \xi_s$). $N(r)$ is plotted as a function of r for densities of (a) $\rho = 0.2$, (b) 0.3, (c) 0.5, and (d) 0.7. Data are the same as those presented in Fig. 3. Dotted lines indicate $\propto r^3$, whereas dashed lines indicate $\propto r^{D_f}$ with (a) $D_f = 2.2$, (b) 2.4, (c) 2.7, and (d) 2.9. At approximately $r = \xi_s$, crossover occurs between $N(r) \propto r^3$ and $\propto r^{D_f}$.

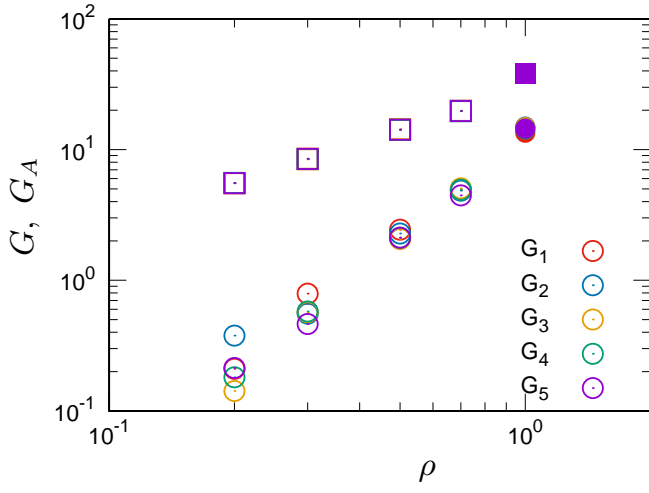


FIG. S3. Five components of shear moduli. G_1 , G_2 , G_3 , G_4 , and G_5 are plotted as functions of ρ . We also plot by squares the corresponding affine shear moduli. Closed symbols represent data of the glass with $\rho = 1.0$.

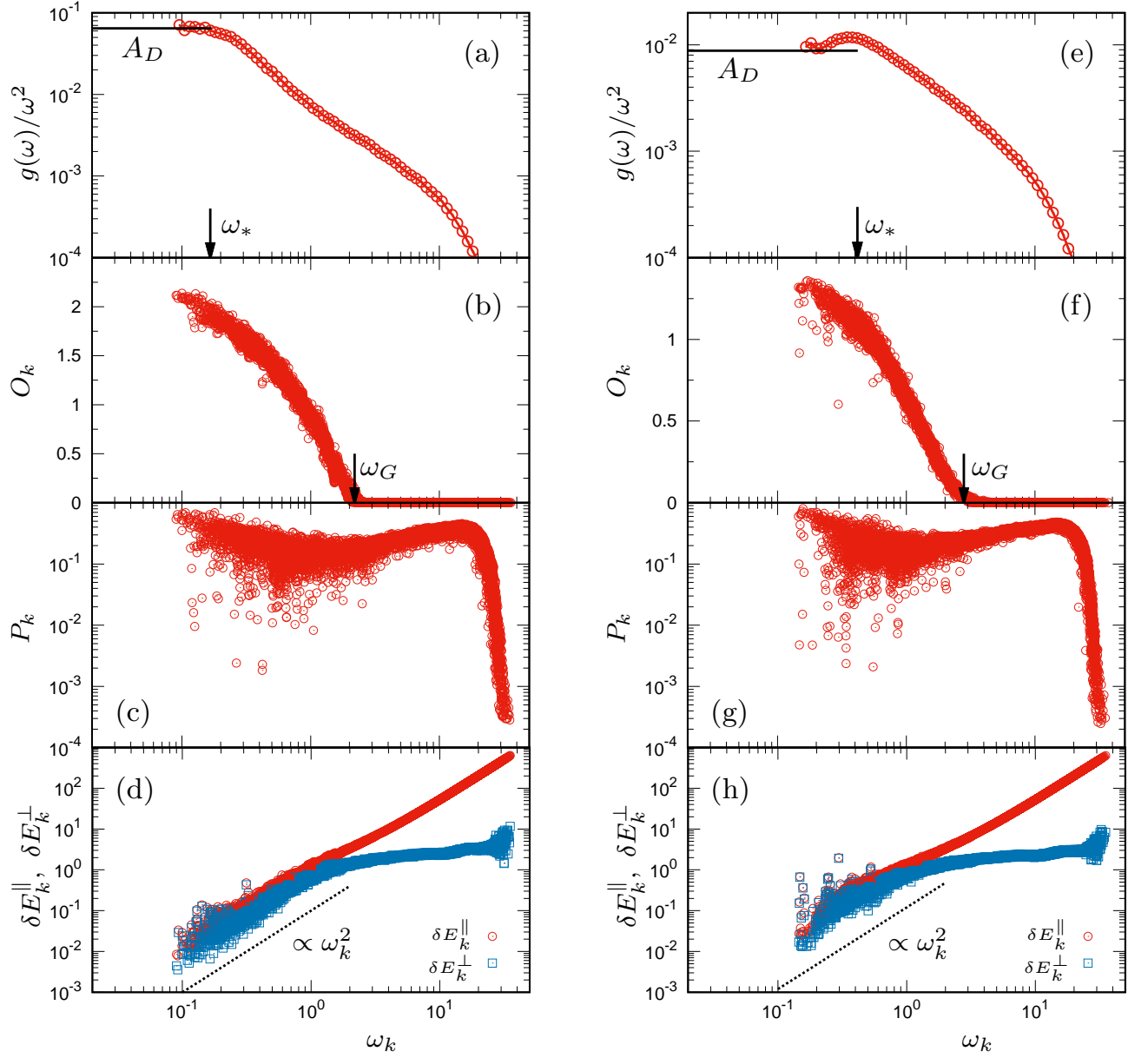


FIG. S4. Characterization of vibrational modes. Plots of (a,e) $g(\omega)/\omega^2$, (b,f) O_k , (c,g) P_k , (d,h) δE_k^{\parallel} , and δE_k^{\perp} of each mode k as functions of ω_k . The left panels of (a) to (d) represent data of the gel with $\rho = 0.3$, and the right panels of (e) to (h) are those of the gel with $\rho = 0.5$. The data of $g(\omega)/\omega^2$ are the same as those presented in Fig. 7(b). The horizontal lines in panels (a,e) present the Debye level A_D . The arrows in (a,e) indicate the frequency ω_* , whereas those in (b,f) indicate ω_G at which O_k becomes zero, $O_k \approx 0$.

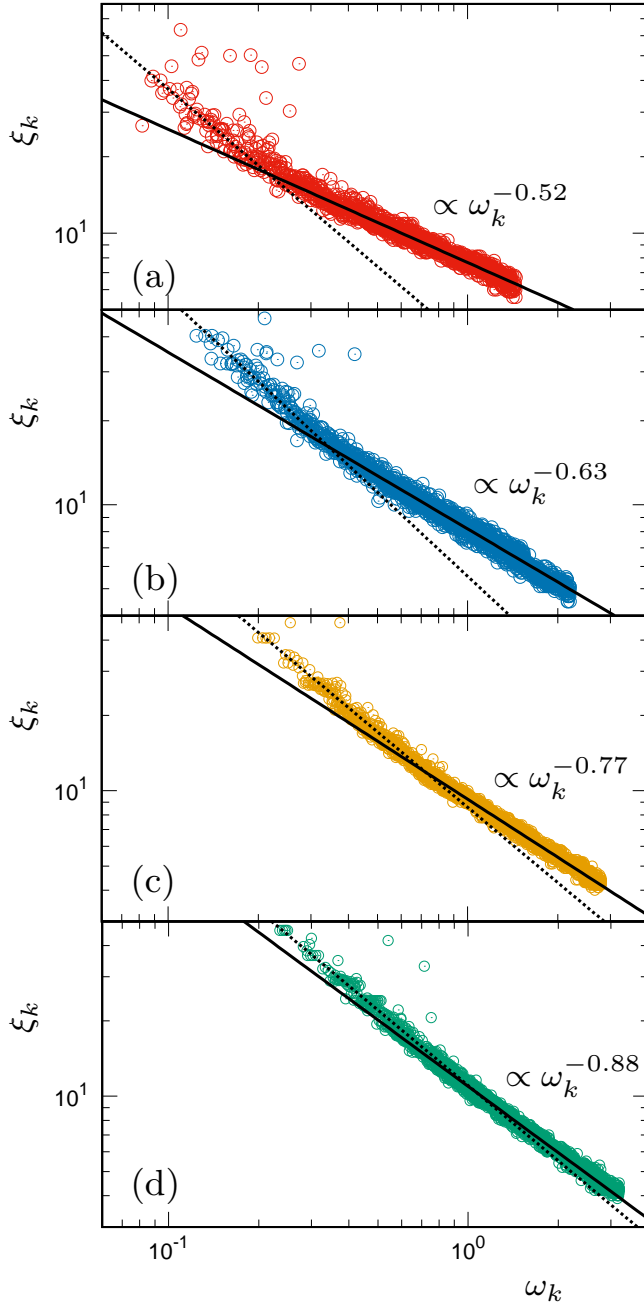


FIG. S5. Exponent $1/a$ of $\xi_k \propto \omega_k^{-1/a}$ (at $\xi_k < \xi_s$). ξ_k is plotted as a function of ω_k for densities of (a) $\rho = 0.2$, (b) 0.3 , (c) 0.5 , and (d) 0.7 . Data are the same as those presented in Fig. 12. Dotted lines indicate $\propto \omega_k^{-1}$, whereas solid lines indicate $\propto \omega_k^{-1/a}$ with (a) $1/a = 0.52$, (b) 0.63 , (c) 0.77 , and (d) 0.88 . At approximately $\omega_k = \omega_c$, crossover occurs between $\xi_k \propto \omega_k^{-1}$ and $\propto \omega_k^{-1/a}$.